U.S. ARMY

U.S. ARMY COMBAT CAPABILITIES DEVELOPMENT COMMAND
CHEMICAL BIOLOGICAL CENTER
ABERDEEN PROVING GROUND, MD 21010-5424

DEVCOM CBC-TR-1863

# Influence of Particle–Polymer Interface on Chemical Transport in Polymer Composites

**Mark J. Varady**
**Brent A. Mantooth**
**Thomas P. Pearl**
**Matthew Browe**
**RESEARCH AND OPERATIONS DIRECTORATE**

**Melissa S. Hulet**
**LEIDOS, INC.**
**Reston, VA 20190-5617**

**Kenneth Strawhecker**
**Alice Savage**
**Jonathan Ligda**
**U.S. ARMY COMBAT CAPABILITIES DEVELOPMENT COMMAND ARMY RESEARCH LABORATORY**
**Aberdeen Proving Ground, MD 21005-5300**

**Adam R. Hinkle**
**DCS CORPORATION**
**Belcamp, MD 21017-1561**

**Melissa L. Sweat**
**DEFENSE THREAT REDUCTION AGENCY**
**Ft. Belvoir, VA 22060-6201**

**December 2023**

Disclaimer

The findings in this report are not to be construed as an official Department of the Army position unless so designated by other authorizing documents.

# REPORT DOCUMENTATION PAGE

| 1. REPORT DATE | 2. REPORT TYPE | 3. DATES COVERED | |
|---|---|---|---|
| | | START DATE | END DATE |
| XX-12-2023 | Final | Oct 2018 | Sep 2021 |

**4. TITLE AND SUBTITLE**
Influence of Particle–Polymer Interface on Chemical Transport in Polymer Composites

| 5a. CONTRACT NUMBER | 5b. GRANT NUMBER | 5c. PROGRAM ELEMENT NUMBER |
|---|---|---|
| | | |
| **5d. PROJECT NUMBER** | **5e. TASK NUMBER** | **5f. WORK UNIT NUMBER** |
| PE 0601102A, VR9 | | |

**6. AUTHOR(S)**
Varady,* Mark J.; Mantooth, Brent A.; Pearl, Thomas P.; Browe, Matthew (DEVCOM CBC); Hulet, Melissa S. (Leidos.); Strawhecker, Kenneth; Savage, Alice; Ligda, Jonathan (DEVCOM ARL); Hinkle, Adam R. (DCS); Sweat, Melissa L. (DTRA)

**7. PERFORMING ORGANIZATION NAME(S) AND ADDRESS(ES)**
Director, DEVCOM CBC; ATTN: FCDD-CBR-PD, APG, MD 21010-5424
Leidos, Inc.; 1750 Presidents Street, Reston, VA 20190-5617
DEVCOM Army Research Laboratory; Aberdeen Proving Ground, MD 21005-5300
DCS Corporation; 4696 Millennium Drive, Suite 450, Belcamp, MD 21017-1561
Defense Threat Reduction Agency; 8725 John J. Kingman Road, MSC 6201, Fort Belvoir, VA 22060-6201

**8. PERFORMING ORGANIZATION REPORT NUMBER**
DEVCOM CBC-TR-1863

| 9. SPONSORING/MONITORING AGENCY NAME(S) AND ADDRESS(ES) | 10. SPONSOR/MONITOR'S ACRONYM(S) | 11. SPONSOR/MONITOR'S REPORT NUMBER(S) |
|---|---|---|
| Surface Science Initiative Program, U.S. Army Combat Capabilities Development Command Chemical Biological Center; 8198 Blackhawk Road, Aberdeen Proving Ground, MD 21010-5424 | DEVCOM CBC | |

**12. DISTRIBUTION/AVAILABILITY STATEMENT**
Distribution Statement A. Approved for public release: distribution unlimited.

**13. SUPPLEMENTARY NOTES**
*Author Mark J. Varady is no longer affiliated with DEVCOM CBC.

U.S. Army Combat Capabilities Development Command Chemical Biological Center (DEVCOM CBC) was previously known as U.S. Army Edgewood Chemical Biological Center (ECBC).

**14. ABSTRACT**
Protective coatings on military assets are complex polymer composites consisting of a high loading of several different particle types to achieve desired coating performance attributes, including resistance to toxic compounds. Chemical mass transport properties at particle–polymer interfaces can differ significantly from those in the polymer bulk, and when interfacial regions overlap at sufficiently high loading, undesirable, interconnected, fast-transport pathways can result. In this work, polyurethane–silica composite films are used as model systems to investigate how interfaces can be tuned to improve the transport properties using particle surface-chemistry modifications. Specifically, silica particles are modified by silanization to alter the interaction with a polyurethane matrix. Atomic force microscopy-based colloidal force spectroscopy on single particles and imaging of cross-sectioned composites were used to assess changes in the particle–polymer interface. Breakthrough measurements for different probe molecules exposed to the composites were performed using Fourier transform infrared–attenuated total reflectance spectroscopy. Comparing how specific modifications to the particle surface influence the nature of the interface and chemical transport is an important step in developing structure–property relationships for chemical transport in polymer composites and rational approaches to controlling transport properties.

**15. SUBJECT TERMS**

| | | |
|---|---|---|
| Polymer composites | Coatings | Atomic force microscopy (AFM) |
| Colloidal force spectroscopy | Chemical transport | Adhesion |

| 16. SECURITY CLASSIFICATION OF: | | | 17. LIMITATION OF ABSTRACT | 18. NUMBER OF PAGES |
|---|---|---|---|---|
| a. REPORT | b. ABSTRACT | C. THIS PAGE | | |
| U | U | U | UU | 58 |

| 19a. NAME OF RESPONSIBLE PERSON | 19b. PHONE NUMBER *(Include area code)* |
|---|---|
| Renu B. Rastogi | (410) 436-7545 |

**STANDARD FORM 298 (REV. 5/2020)**
*Prescribed by ANSI Std. Z39.18*

Blank

## PREFACE

The work described in this report was authorized by the Surface Science Initiative Program at the U.S. Army Combat Capabilities Development Command Chemical Biological Center (DEVCOM CBC; Aberdeen Proving Ground, MD) under project number PE 0601102A, VR9. The work was started in October 2018 and completed in September 2021.

At the time this work was performed, the U.S. Army Combat Capabilities Development Command Chemical Biological Center (DEVCOM CBC) was known as the U.S. Army Edgewood Chemical Biological Center (ECBC).

The use of either trade or manufacturers' names in this report does not constitute an official endorsement of any commercial products. This report may not be cited for purposes of advertisement.

This report has been approved for public release.


## Acknowledgments

The authors acknowledge the DEVCOM CBC Decontamination Sciences Branch members for their hard work and assistance with the execution of this technical program.

Blank

## CONTENTS

## FIGURES

## TABLE

Blank

# INFLUENCE OF PARTICLE–POLYMER INTERFACE ON CHEMICAL TRANSPORT IN POLYMER COMPOSITES

## 1. INTRODUCTION

The aim of this work was to provide an improved understanding of chemical transport in polymer composites by investigating the role of the particle–polymer interface. The motivation for performing this work stemmed from the desire to improve the chemical resistance of military paint coatings. These coatings are complex polymer composites that consist of a high loading of many different types of polydisperse particles in a polymer matrix, to achieve all of the required functions of the coating (e.g., camouflage, low gloss, or corrosion resistance). Prior coating formulation efforts have not made chemical resistance a central focus, and the complex nature of these coatings obscures a fundamental understanding of how to make improvements. In this work, a model polymer composite system was used that consists of a single monodisperse, chemically uniform particle type to enable a basic study aimed at determining how variations in polymer interactions with embedded particles influence chemical mass transport in composites. Background information on relevant coating systems, the rationale for this investigation, and a review of prior research on the effect of the particle–polymer interface on macroscopic composite properties are provided here.

### 1.1 Chemical Resistance of Paint Coatings

Protective coating systems for military assets must resist corrosion, present low-gloss and camouflage surfaces, be robust and durable, as well as adhere to chemical warfare agent (CWA) resistance requirements under a wide array of use conditions. Recently, a revised method for quantifying chemical agent resistance of protective coatings was developed in which the mass of CWA retained on or within the coating is measured after deposition of a liquid CWA droplet followed by removal of any remaining bulk liquid CWA via a water rinse or immersion.[1] Using this new method, more stringent targets for agent resistance have been established, and future formulations must not only meet those new standards but continue to satisfy all other requirements. Often there are tradeoffs; it is not trivial to formulate a paint coating that improves on one requirement while retaining conformance on all others.

Multiple recent efforts have sought enhanced mechanistic understanding of chemical transport on the surface and in the bulk of coatings, to build a knowledge base for improved coatings formulation from the bottom up. An important retention mechanism is liquid spreading and capillary stabilization in the surface roughness of protective paint topcoats.[2] On the micron length scale, surface roughness ensures diffuse light reflection and a low-gloss coating, meeting an important requirement. However, when a liquid wets the surface, it can be pulled into the roughness features via strong capillary forces that enhance spreading and also make removal more difficult. The liquid chemical on the coating surface can enter into the polymer binder via a solution-diffusion mechanism.[3,4] In this framework, the chemical dissolves into the polymer matrix and diffuses along a chemical potential gradient within the polymer matrix. This occurs when (1) it is thermodynamically favorable for a measurable quantity of chemical to absorb (dissolve) in the polymer matrix,[5–7] and (2) there is sufficient mobile free

volume to accommodate motion of a penetrant molecule between polymer chains.[8–10] From these considerations, it is immediately clear that chemical resistance can be improved by reducing the spacing and mobility of the polymer chains and/or ensuring they are chemically incompatible with the chemicals of interest (i.e., mixing is not thermodynamically favored). However, both of these changes would also impact the mechanical properties of the coating and could negatively impact durability and toughness by making the coating more brittle.[11–13] Furthermore, any solid inclusions (particles) can also influence the chemical transport. It is this effect that is further explored in this work. In the ideal case, the particles do not alter the surrounding polymer matrix, and the effective diffusivity of the composite is lower than that of the pure polymer due to the particles acting as impermeable barriers.[14] Departure from this ideal case can occur in either direction, increasing or decreasing the effective diffusivity of the chemical in the composite, depending on how the mobile free volume of the polymer is influenced by the presence of the particle surface.

In past work, the CWA or simulant breakthrough dynamics in protective coatings were measured. In one method, the coating was contaminated by placing a liquid CWA or simulant droplet on the surface, allowing for the liquid to interact with the paint for a given duration, then cleaving to expose the contaminated cross section. This allowed for imaging of the cross-section morphology with scanning electron microscopy (SEM) as well as concurrent mapping of elemental abundance using spatially resolved energy-dispersive spectroscopy (EDS).[15,16] Any elements that exist solely in a CWA simulant and not in the coating (e.g., S and Cl for 2-chloroethyl ethyl sulfide, and P for dimethyl methylphosphonate) indicate the presence of that compound, and depth profiles of chemical intensity in the topcoat (and corresponding pure polymer binder) were developed. This revealed that the CWA simulant penetrated the entire depth of the topcoat (~50 μm) within minutes after exposure, but it progressed much more slowly in the pure polymer and did not penetrate the entire depth after 1 h of exposure. This indicated that the particles have a significant impact on chemical transport in these coatings, and the SEM images revealed possible defects at the particle interfaces that would explain the observations.

In another method, Fourier transform infrared (FTIR) spectroscopy was used with attenuated total reflectance (ATR): the coating was placed in intimate contact with an ATR element and exposed to a chemical on the other side.[17] By monitoring the intensity of the IR peaks associated with the CWA or simulant, a breakthrough curve can be constructed and used to fit diffusion models. This was done for paint coatings with different pigments as well as the pure polyurethane (PU) binder. As was shown in the SEM–EDS experiments, the breakthrough dynamics were about an order of magnitude slower in the pure polymer as compared with the full coatings with high particle loading (Figure 1). It is clear that the presence of the particles has a significant impact on the macroscopic transport behavior of chemicals within these paint coatings. An improved understanding of the variation in properties from the polymer bulk to the particle interface is necessary for rational engineering of coatings for improved chemical resistance.

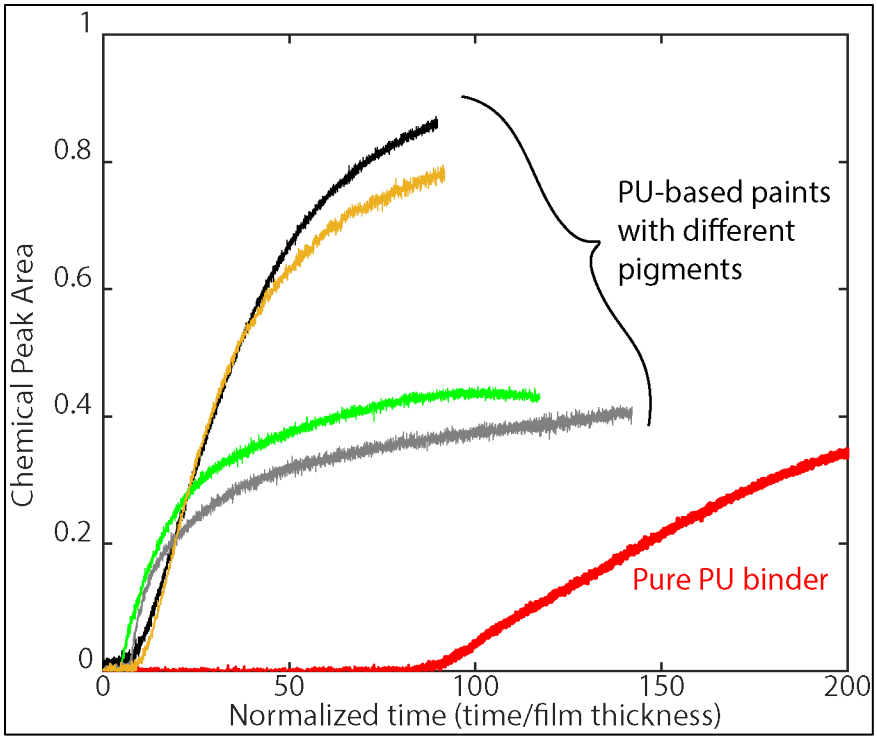


Figure 1. Comparison of chemical breakthrough dynamics in a pure PU binder (red line) and in PU-based paint coatings with different pigments (gray, green, tan, and black lines).

## 1.2 Prior Work on Influence of Particle–Polymer Interface in Composites

The importance of the interfacial region in polymer composites has been recognized in connection with other applications, particularly for macroscopic mechanical, electrical, and thermal properties. Several studies have linked strong attractive interactions between the polymer and particle to increased glass-transition temperature ($T_g$) due to restriction of polymer chain mobility near the particle interface. For example, strong hydrogen bonding between hydroxyl groups on the surface of silica particles with either polymethyl methacrylate (PMMA) or poly(2-vinyl pyridine) (P2VP) results in a higher $T_g$ in the corresponding composites compared with the pure polymers.[18] More recent studies using differential scanning calorimetry (DSC) in P2VP–silica composites[19] and broadband dielectric relaxation spectroscopy (BDS) in PMMA–silica composites[20] have revealed heterogeneous chain dynamics, providing further evidence of decreased chain mobility near the particle interface in these systems. Conversely, weak or poor interactions between the polymer and particle surface can lead to a decrease in the $T_g$ of the composite, as shown for polystyrene (PS)–silica composites.[18,21] Polymer chain length and particle size have also been shown to impact the nature of the interfacial region.[22,23]

The interfacial region can have a strong influence on the properties of polymer composites, and it is thus vital to understand when engineering functional composite materials. For this reason, much attention has been given to chemically modifying the interface to help achieve the desired properties. In high-strength composites, effective stress transfer at the

interface is required to attain the maximum benefit from the solid additive. Silane treatment of the solid is one widely used method for accomplishing this[24,25] and has been used to strengthen cellulose–epoxy,[26] glass fiber–epoxy,[27] and polypropylene–zeolite[28] composites to name a few. Grafting polymer chains on the surface of the solid inclusions can also improve compatibility with the polymer matrix, and this has been demonstrated by grafting PS chains on silica[29] and epoxy chains onto graphene oxide.[30] The connectivity of the interfacial regions throughout the composite can also have an enormous impact on macroscopic properties and must also be considered.[31]

Development of experimental techniques for probing the interface has also been important for establishing structure–property–processing relationships for composite materials. In addition to the bulk characterization methods such as DSC and BDS mentioned above, small-angle neutron scattering has also been used to detect variations in polymer structure between the interface and bulk in composites.[22,32] Neutron reflectometry is able to directly probe the polymer–solid interface, but it requires the use of idealized planar two-dimensional model systems to approximate the interface in the actual composite.[33,34] Positron annihilation lifetime spectroscopy (PALS) is used to measure the free volume in polymers, which is one of the primary factors governing the diffusion coefficient of small penetrant molecules. PALS has been employed to infer variations in free volume at the solid interface in polymer composites such as PMMA–alumina[35] and PS–gold.[36]

### 1.3 Goals of This Work

In view of the prior work on polymer composites, one possible explanation for the degradation of chemical resistance between pure polymers and fully formulated paint coatings is the existence of an interfacial region at the particle–polymer interface with increased free volume, and thus increased chemical diffusivity as compared to the bulk polymer. When the solids loading is sufficiently high, these interfacial regions can overlap and result in a connected network of fast transport pathways for chemical species to traverse. This is shown schematically in Figure 2.

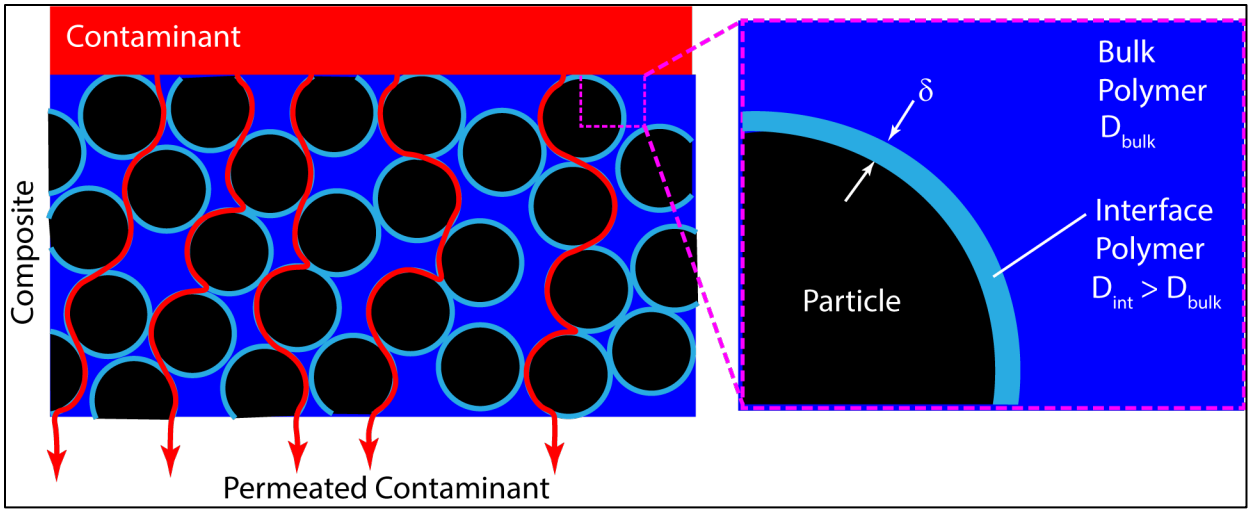


Figure 2. Possible chemical permeation pathways in high solids loading polymer composite with non-ideal particle–polymer interface. Overlap of particle interface regions with higher free volume and higher chemical diffusivity relative to the bulk polymer ($D_{int} > D_{bulk}$) results in a percolated network of fast transport pathways through the composite.

To facilitate a basic study of this proposed mechanism, attention was confined to a model system consisting of monodisperse silica particles in a PU matrix. The use of silica particles enabled relatively easy modification of the particle surface chemistry via treatment with commercially available silane chemistries chosen to vary the hydrogen bonding strength with the surrounding polymer matrix. PU was used as the polymer matrix because it is used as the binder in some protective coating systems.

This work included atomic force microscopy (AFM)-based techniques to directly probe the particle–polymer interface in the PU–silica composite system to provide information on the particle–polymer interaction strength and the local polymer properties at the particle interface. Colloidal force spectroscopy, which is a type of nanoindentation measurement, was used to measure the particle–polymer interaction strength. This is a widely used technique to study adhesion forces in which a particle (usually spherical) attached to the end of an AFM cantilever is brought into contact with a surface; the force required to separate the two (adhesion force, $F_{adh}$) is measured from the maximum deflection of the cantilever.[37,38] AFM cantilevers with the particle attached are referred to as *colloidal probes*. The general steps in the force spectroscopy procedure are shown in Figure 3.

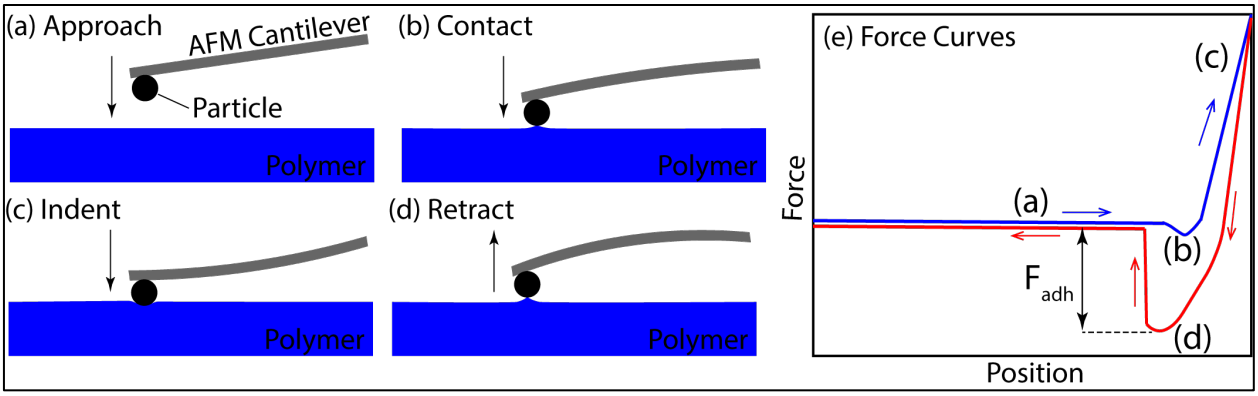


Figure 3. Colloidal force spectroscopy with AFM showing spherical particle on the end of an AFM cantilever and the snapshots at various points in the process. (a) Approach of the probe to the polymer surface; (b) probe making contact with the surface; (c) indentation of probe into polymer surface; and (d) retraction of probe resisted by attractive forces between particle and polymer, causing cantilever deflection before separation from surface. (e) Measured force curves shown during approach (blue) and retraction (red). Distance between particle and surface decreases from left to right on the position axis until position (b).

AFM was also used to perform high-resolution spatial mapping of viscoelastic properties over cross-sectioned PU–silica composites. This method is attractive because one can directly observe the influence of particle–polymer chemistry and processing conditions on the local interface properties and, in turn, how these correlate with the bulk composite mechanical behavior. This technique has been used in prior studies, for example, Nguyen et al.[39] measured the interfacial region in composites consisting of carbon black particles suspended in either styrene–butadiene rubber or isoprene rubber using amplitude modulation AFM. They measured an interfacial region between 20 and 30 nm and determined that the interface in the isoprene rubber composite exhibited a higher loss tangent, which aligned with bulk dynamic mechanical analysis (DMA) measurements. In another example, the peak force quantitative nanomechanical mapping method was applied to carbon fiber–epoxy composites to show that the interface thickness increased from 45 to 76 nm after aging under high-temperature and humid conditions, thereby providing an explanation for observed bulk behavior.[40]

The effect of silica surface-chemistry modification on the particle–polymer interface was assessed by the AFM-based methods and compared with corresponding changes in the permeation rate of a probe molecule (methanol [MeOH]) through the PU–silica system, as a function of particle loading using FTIR-ATR. It was expected that the permeation rate would drastically increase above a critical loading level (i.e., percolation threshold) for silica surface chemistries resulting in weak particle–polymer interaction and an interfacial region with high free volume.

# 2. MATERIALS AND METHODS

## 2.1 Materials

PU was synthesized by the U.S. Army Combat Capabilities Development Command Army Research Laboratory (DEVCOM ARL; Aberdeen Proving Ground, MD) and is described in a previous publication.[17] Carbonated diglycidyl ether of bisphenol A (10.84 g, 25.30 mmol), diaminohexane (2.94 g, 25.30 mmol), and triazabicyclodecene (0.352 g, 2.53 mmol) were dissolved in 25 mL of *n*-methyl pyridine and allowed to stir at room temperature for 24 h. The reaction mixture was diluted with tetrahydrofuran (THF) and added dropwise to 600 mL of stirred 1:1 deionized (DI) water–MeOH. The resulting precipitate was collected by vacuum filtration and dried under high vacuum. The polymer was redissolved in THF, precipitated in 1:1 DI $H_2O$–MeOH, and collected by vacuum filtration (2×). The polymer was completely dried at 50 °C under high vacuum to yield 11.32 g (82%) of polymer with a $M_n$ (via size exclusion chromatography) of 33.8 kDa and a $T_g$ (via DSC) of 65 °C.

Silica and functionalized silica particles obtained from Polysciences, Inc. (Warrington, PA) included 0.5 and 5 μm silica (catalog nos. 25342 and 25348), carboxyl functionalized silica (catalog nos. 24753 and 24755), and amine-functionalized silica (catalog nos. 24756 and 24758). Some bare silica particles were functionalized with various alkoxysilanes (Gelest; Morrisville, PA) in aqueous alcohol solution. The silica particles were first washed by dispersing ~0.1 g in 1.5 mL of ethanol (EtOH), and mixed at a speed of 18,000 rpm (D160 homogenizer; Scilogex; Rocky Hill, CT) for 5 min, sonicated for 15 min, centrifuged for 20 min at 4000 rpm, then pulled off the supernatant EtOH. The washing procedure was repeated three times prior to silanization to remove any impurities from the particle surface. The solution was dried in a vacuum oven at 70 °C at least overnight. Following the procedure recommended by Gelest, ~4 wt% silane solution was made by adding the silane dropwise with mixing into a 95% EtOH–$H_2O$ solution adjusted to pH ~5 by addition of acetic acid. After it was mixed for 5 min, 1.5 mL of the solution was added to the washed silica particles. This solution was mixed for 5 min at 18,000 rpm, sonicated for 15 min, and centrifuged for 20 min at 4000 rpm. The washing procedure described above was repeated three times to remove excess silane not bound to the silica surface. The silanized silica particles were placed in a vacuum oven at 110 °C for at least 24 h, to cure the silane and dry the particles.

## 2.2 Sample Preparation

### 2.2.1 Composite Preparation

Silica–polymer composites were created by dispersing 0.5 μm silica particles in cyclopentanone using the Scilogex D160 homogenizer operating on setting 1 (~8000 rpm) for 30 s. An amount of the particle suspension was added to 100 mg/mL PU in cyclopentanone solution to achieve the desired particle–polymer mass ratio. During the project, it was recognized that the original mixing procedure resulted in relatively poor dispersion of silica in the PU matrix. As a result, a revised mixing procedure was developed to improve the solids dispersion. Results are presented for both mixing procedures, as it is illustrative of the effect of processing conditions on the properties of the final composite material.

1. The silica–PU–cyclopentanone mixture was homogenized with the Scilogex D160 homogenizer operating on setting 1 (~8,000 rpm) for 30 s.
2. The silica–PU–cyclopentanone mixture was homogenized with the Scilogex D160 homogenizer operating on setting 2 (~128,000 rpm) for 15 min and was followed by bath sonication for 15 min.

For chemical breakthrough measurements, 100 µL of the particle–polymer–solvent mixture was spread onto an ATR crystal (germanium, 45°, 80 mm × 10 mm × 4 mm; Pike Technologies; Madison, WI), and an additional 100 µL of the mixture was added on top. The coated crystal was placed in a dry $N_2$ environment at atmospheric pressure for approximately 30 min, then it was placed in a vacuum oven at 70 °C for 24 h. The dry composite films prepared on ATR crystals were nominally 20 µm thick. Free films of composites for AFM imaging samples were prepared by first pouring 4 mL of the particle–polymer–solvent mixture into a 2 in. diameter Teflon dish. The dish was kept in a dry $N_2$ environment at atmospheric pressure overnight and then placed in a vacuum oven at 70 °C for 24 h. The dry composite films prepared for AFM imaging were nominally 0.5 mm thick, which is sufficient to enable microtoming.

### 2.2.2 Cross Sectioning of Composite Films

Composite free films were cross sectioned using a Leica EM UC7 ultramicrotome (Leica Microsystems; Deerfield, IL). A ~500 µm thick PU silica composite was rough cut to expose the cross section. The samples were cooled to –80 °C and cut in 500 nm slices with a glass knife, then finishing cuts of 150 nm slices were made using a diamond knife (45°, Diatome; Hatfield, PA).

## 2.3 Measurement Techniques

### 2.3.1 Colloidal Probe Preparation

Some of the colloidal probes used in this work were purchased from Novascan Technologies (Boone, IA). These included 5 µm silica, amine ($NH_2$)-functionalized silica, and carboxyl (COOH)-functionalized silica, all with a nominal spring constant ($k$) of 16 N/m.

In-house colloidal probes were also prepared by attaching 5 µm silica particles to tipless AFM cantilevers using an epoxy-based UV-cure adhesive. First, silica particles were dispersed on a glass slide to make them accessible for attachment. A 1 in. glass slide was sonicated in a MeOH bath for 15 min, dried in a dry $N_2$ stream, and then placed in a UV–ozone cleaner for 20 min. A 35 µL droplet of ~0.01 mg/mL silica particles in MeOH was deposited on the clean glass slide and dried in a 70 °C oven for at least 1 h to dry the particles.

To place epoxy on tipless cantilevers in preparation for silica particle attachment, a small droplet of UV-cure adhesive (Flashbond UV-6502CL; Epoxyset; Woonsocket, RI) was spread into a thin film on the surface of a Au-coated glass slide by blowing with a dry $N_2$ stream at 40 psi from a 1/8 in. OD plastic tube. A small quantity of the adhesive (≤2 µm diameter) was placed on the end of a tipless AFM cantilever (AppNano ACLA-TL or ACTA-TL; Applied

NanoStructures; Mountain View, CA) by locating the edge of the adhesive film, lowering the cantilever into the adhesive near the edge, then moving the AFM sample stage with the barrel micrometer to drag the cantilever from the adhesive onto the dry part of the surface to remove any excess adhesive. The glue was partially cured by exposure to a 365 nm UV source of 500 mW/cm$^2$ intensity (Cool Cure 365 Lite; American Ultraviolet; Lebanon, IN) at a distance of 1 cm for 2 s, which prevented encapsulation of the colloidal particle upon attachment. The size of the adhesive spot on the cantilever was checked using the high-magnification objective lens on a Leica DVM6 digital microscope.

An inverted setup was constructed to attach colloidal particles onto the adhesive-coated AFM tip, in which the silica particle-decorated glass slide was held upside down and offset from the DVM6 microscope stage. This allowed for a clear view of the cantilever alignment with a target particle upon attachment, as shown in Figure 4. The cantilever holder was mounted on an arm connected to a three-axis positioning stage that moved independently from the microscope stage. To perform the particle attachment, the microscope stage was moved to find a particle within the field of view, and the stage was raised to allow for positioning of the cantilever. The positioner was used to bring the cantilever tip within the field of view, then the arm was slightly retracted along the *z* axis before the microscope stage was lowered to bring the particle of interest back into focus. The *z* position of the cantilever was slowly adjusted to bring it closer to the particle, while the *x* and *y* positions were adjusted to align the particle with the adhesive dot on the cantilever. After successful particle attachment, the adhesive was cured by exposure to UV light for 25 s while the source was manually moved to expose the adhesive and particle from all angles. The completed colloidal probes were placed in a 70 °C oven overnight to fully cure and dry the adhesive.

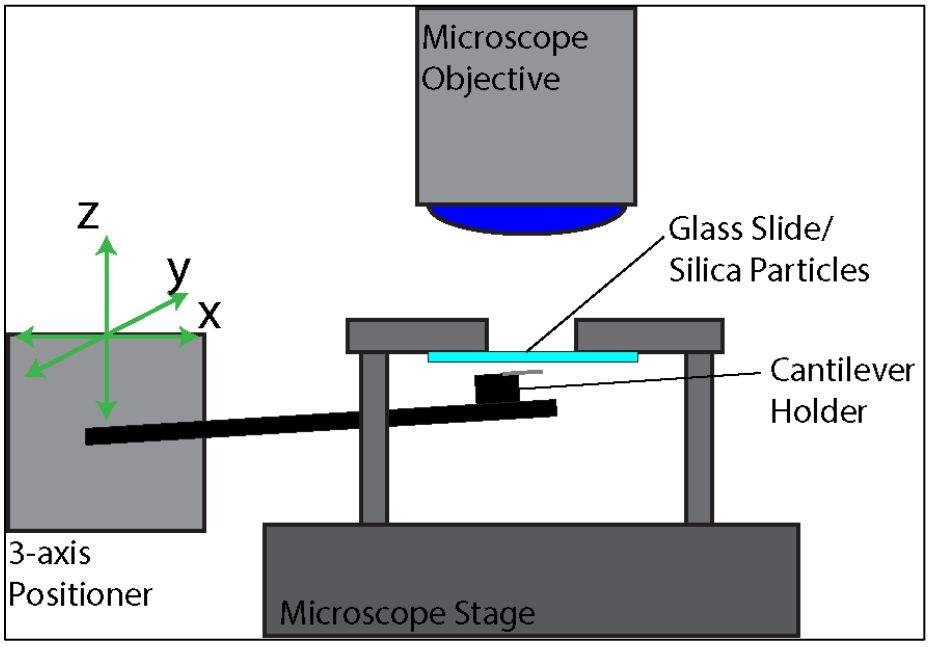

Figure 4. Setup used to manufacture colloidal probes.

### 2.3.2 Chemical Breakthrough

Details of the chemical breakthrough experiments have been described in previous publications.[17,41] In this work, the primary penetrant of interest was MeOH, and a controlled MeOH vapor concentration was created by flowing dry $N_2$ gas through a custom blown, glass saturator cell (Glassblowers.com; Alloway, NJ) that was saturated with liquid MeOH. The vapor activity delivered (i.e., ratio of partial pressure to vapor pressure) was set to 0.1 by combining the saturated MeOH vapor flow with dry $N_2$ and setting the corresponding mass flow controllers in the desired ratio with a total flow rate of 50 sccm in all cases. This flow was passed over the top of the polymer-coated Ge ATR crystal, and IR light was shone through the backside of the crystal, creating an evanescent wave at the polymer–crystal interface. Monitoring the intensity of the reflected infrared light as a function of wavelength allows for the detection of species with corresponding absorption bands. Because the evanescent wave penetrates less than 600 nm into the polymer (as determined by the ATR crystal cut and geometry, the IR wavelength, and the difference in indices of refraction between the Ge ATR crystal and the polymer), this measurement only detects species near the polymer–crystal interface. Integration over the absorption bands corresponding to MeOH allows for quantification of the amount of MeOH absorbed reaching the polymer–ATR crystal interface as a function of time. A schematic of the experimental apparatus and resulting data is shown in Figure 5. All measurements were performed isothermally with saturator cells and an ATR flow cell held at 40 °C.

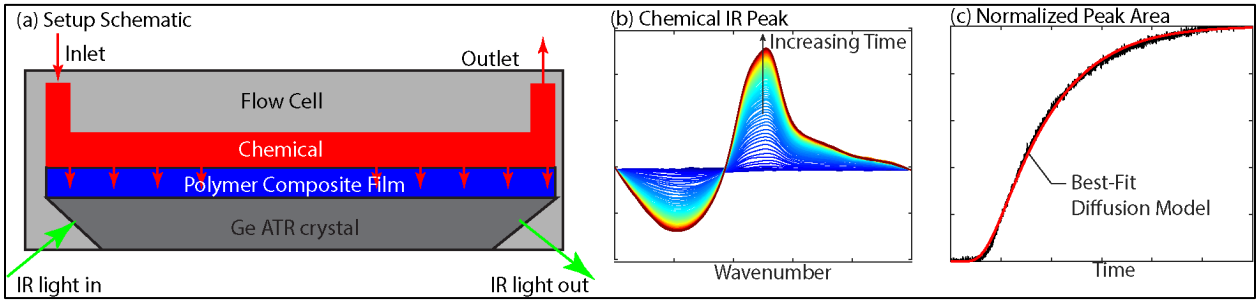


Figure 5. (a) FTIR-ATR setup for measuring chemical breakthrough dynamics; (b) example evolution of IR peak associated with the chemical (blue, initial time; red, final time); and (c) plot of peak area versus time yielding a breakthrough curve fit with a diffusion model (red curve).

### 2.3.3 Standard AFM Colloidal Force Spectroscopy

Colloidal probe AFM was applied to measure the adhesion force between a single 5 µm silica particle and a PU surface using a Nanosurf FlexAFM (Woburn, MA). The deflection sensitivity of the colloidal probe was calibrated before it was used for adhesion force measurement: the photodetector voltage was measured as the cantilever's $z$ position was increased to 500 nm while the particle was in contact with the surface of a silicon wafer. Assuming the silicon wafer is rigid, the change in $z$ position is equal to the cantilever deflection ($\delta$), thereby providing a relationship between voltage and displacement. The spring constant of the cantilever ($k$) was determined using the thermal method available in the software, and the force at the tip of the cantilever was computed from the Hooke's law analogue, $F = k\delta$.

In the standard adhesion force measurement, the temperature of the AFM sample stage was set to the desired value using the Nanosurf temperature controller stage add-on. The temperature was allowed to equilibrate for approximately 15 min before the colloidal probe was brought into contact with the polymer surface. A Type J thermocouple (model SA-1J; Omega Engineering; Norwalk, CT) was placed in close proximity to the sample to verify that the sample temperature was in agreement with the controller setpoint (typically within 1 °C). The advanced force spectroscopy measurement module of the AFM was used to set the forward (approach toward the sample) and backward (retract from the sample) *z* range, the stop force above which the forward motion stops, and the forward and backward velocities. The force spectroscopy settings included a 2 μm *z* range and 1 μm/s velocity in both the forward and backward directions and a 100 nN stop force unless otherwise stated. Force curves were acquired over 25 equally spaced points in a 100 μm × 100 μm grid unless otherwise stated, and these were used to perform statistical analysis. Typically, adhesion force was measured from 40 to 90 °C in 10 °C increments for each sample, which spans $T_g$ for the PU used in this work (~65 °C).

### 2.3.4 AFM Phase-Contrast Imaging

Phase-contrast imaging is standard tapping mode AFM, in which a high stiffness cantilever (e.g., AppNano ACLA-TL, with the following nominal values: $k$ of 58 N/m, $f$ of 190 kHz, and $R_{tip}$ of 10 nm) is oscillated at a fixed amplitude near the cantilever resonance, and the z position is adjusted to maintain this amplitude as the tip scans over the sample surface. Depending on material stiffness and tip-sample interaction, the cantilever oscillation is phase shifted from the drive signal. Thus, the phase shift provides a map convolving material and surface variations that can aid in distinguishing different regions of the sample.

### 2.3.5 AFM Amplitude Modulation–Frequency Modulation (AM–FM) Viscoelastic Mapping

AM–FM viscoelastic mapping was also performed using the Asylum Research MFP-3D AFM (Oxford Instruments; Goleta, CA) as described elsewhere.[42,43] Here, in addition to the standard AM tapping mode operating at the fundamental frequency, the cantilever is also excited at its second harmonic but at a much lower amplitude, so it does not interfere with the fundamental. In most cases, the free vibration amplitude measured by the photodetector was set to 1–2 V for the fundamental and 0.015–0.025 V for the second harmonic. The second harmonic frequency is modulated to maintain its vibration on resonance (i.e., the phase is 90°). Additionally, the drive voltage for the second harmonic is continuously adjusted to maintain a constant oscillation amplitude. Shifts in frequency are related to local sample stiffness such that greater positive-frequency shifts indicate increased stiffness.

To achieve thermal equilibrium, the cross-sectioned samples were placed on a temperature-controlled stage for at least 15 min before measurements were made. After the initial tuning of the cantilever, the tip was moved in close proximity to the surface (~100 nm) before a second cantilever tune was performed. This procedure ensures that the cantilever is operated on its resonance, which is critical to obtaining useful viscoelastic information from the second harmonic.

## 3. RESULTS

### 3.1 IR Spectra of PU–Silica Composites

IR spectra of PU–silica composites prepared using the first mixing procedure (1 min homogenization only, see Section 2.2.1) and cast on horizontal attenuated total reflectance (HATR; Pike Technologies) crystals are shown in Figure 6 for particle loadings ranging from 0 to 50 wt%. As expected, the intensity of the primary silica peak at 1070–1100 $cm^{-1}$ (Si–O–Si stretch) increased while the intensities of main PU peaks at 1230–1240 $cm^{-1}$ (C–O stretch), 1510–1540 $cm^{-1}$ (amide), and 1700–1720 $cm^{-1}$ (C=O stretch) decreased as the particle loading was increased. The spectrum for liquid-phase MeOH was also shown to identify the penetrant peaks that would be useful for analysis (i.e., isolated from the PU and silica peaks).

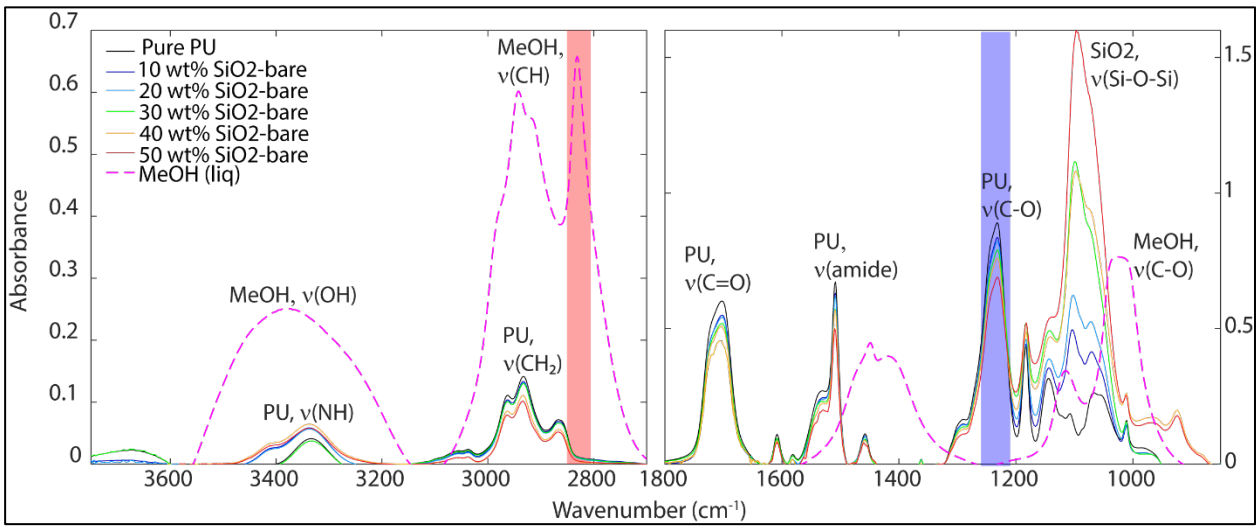


Figure 6. IR spectra of PU-unfunctionalized silica composites prepared using original mixing procedure at various particle loadings: 0 wt% (black), 10 wt% (dark blue), 20 wt% (cyan), 30 wt% (green), 40 wt% (orange), and 50 wt% (red). IR spectrum of liquid-phase MeOH is also shown (magenta). Red and blue shaded regions indicate the MeOH and PU bands to quantify breakthrough and polymer swelling, respectively.

IR spectra obtained for PU-silica composites prepared using the revised mixing protocol (15 min homogenization followed by 15 min bath sonication; see Section 2.2.1) and cast on HATR crystals are shown in Figure 7. The peak intensities qualitatively follow the same trends with particle loading for both mixing procedures. It was also observed that the silica peak intensity was generally higher and the polymer peak intensities were lower at a given particle loading for the revised mixing procedure. This may be an indication that the more-thorough mixing procedure resulted in improved dispersion of the silica particles in the composite. MeOH has a peak at 2830 $cm^{-1}$ that does not significantly overlap with peaks for the PU-silica composite, as shown by the red-shaded region in Figures 6 and 7. Similarly, the PU peak at 1230 $cm^{-1}$ can be used to quantify changes in polymer matrix density, as indicated by the blue-shaded regions in Figures 6 and 7.

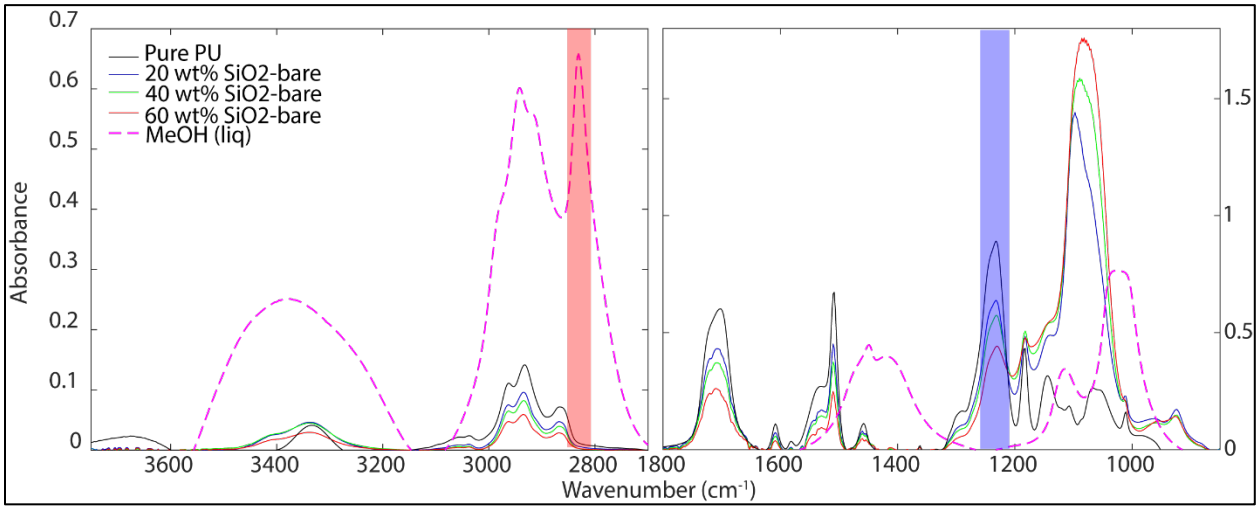


Figure 7. Infrared spectra of PU-unfunctionalized silica composites prepared with revised mixing procedure at various particle loadings: 0 wt% (black), 20 wt% (blue), 40 wt% (green), and 60 wt% (red). The IR spectrum of liquid-phase me MeOH thanol is also shown (magenta). Red and blue shaded regions indicate the MeOH and PU bands to quantify breakthrough and polymer swelling, respectively.

## 3.2 Chemical Breakthrough Dynamics

The procedure to compute breakthrough curves was as follows:

1. Perform a baseline correction on each spectrum in the time series by fitting a cubic spline to the baseline and subtracting that from the spectrum in MATLAB (Baseline Fit, v.1.0, MathWorks File Exchange).
2. Compute a reference spectrum by averaging over the individual spectra at the beginning of each experiment before introduction of the chemical to the flow cell (typically $t_1$ = 30 min to $t_2$ =60 min):

$$A_{\mathrm{ref}}(\nu) = \frac{1}{\Delta t}\int_{t_1}^{t_2} A(\nu,t)\mathrm{d}t \tag{1}$$

3. Compute a difference spectrum at each time point by subtracting the reference spectrum from each spectrum in the time series:

$$A_d(\nu,t) = A(\nu,t) - A_{\mathrm{ref}}(\nu) \tag{2}$$

4. Integrate each difference spectrum in the time series from $\nu_1$ = 2800 cm$^{-1}$ to $\nu_2$ = 2860 cm$^{-1}$ (corresponding to MeOH as described above) to obtain absorbance band area as a function of time, which is the breakthrough curve:

$$\mathrm{Area}(t) = \int_{\nu_1}^{\nu_2} A_d(\nu,t)\mathrm{d}\nu \tag{3}$$

The process is illustrated for MeOH breakthrough in pure PU in Figure 8.

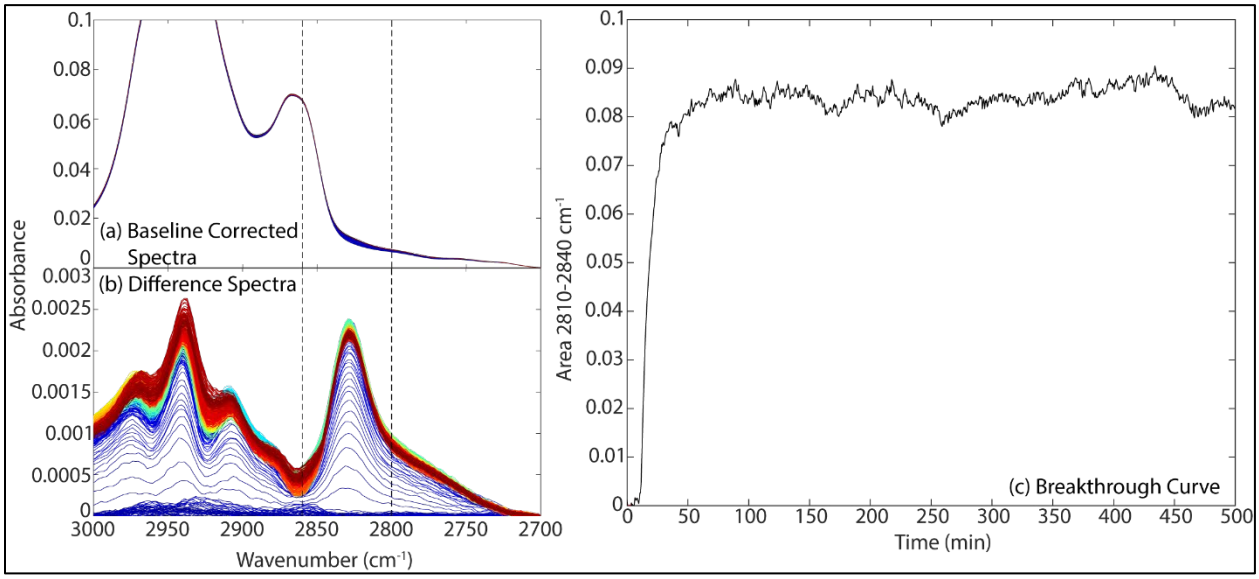


Figure 8. Steps involved in computing a breakthrough curve for MeOH diffusing through a pure PU film cast on a HATR crystal. (a) A baseline correction is applied to all spectra in the time series, (b) difference spectra are computed by subtracting each baseline-corrected spectrum from a reference (average before MeOH is introduced to the flow cell), and (c) breakthrough curve is obtained by computing the area for each difference spectrum between 2800 and 2860 $cm^{-1}$. Line colors indicate relative time from the beginning of the experiment; blue corresponds to early times and red to later times.

To once again illustrate the impact of mixing on the resulting properties of the composite, the breakthrough curves for MeOH at various loading levels of unfunctionalized silica are compared for the original and revised mixing protocols in Figure 9. The breakthrough dynamics of MeOH were clearly faster at a given silica loading level for the composites prepared with the original mixing procedure, as evidenced by visual comparison of the breakthrough curves in Figure 9 (a) and (b). Because the silica particles act as barriers to MeOH diffusion, better dispersion of the particles resulting from the revised mixing procedure led to slower breakthrough dynamics. Also, there was no evidence of increased MeOH diffusion rates at the higher loadings caused by overlap of the high free-volume interfacial regions that resulted from poor particle–polymer interactions. On the other hand, the poor silica dispersion resulting from the original mixing procedure caused particle agglomeration and reduced the specific surface area of the silica particles in the PU matrix (particles in the interior of an agglomerate do not contribute). This led to a reduced transport barrier effect, and the composites exhibited breakthrough dynamics similar to those for the pure PU matrix.

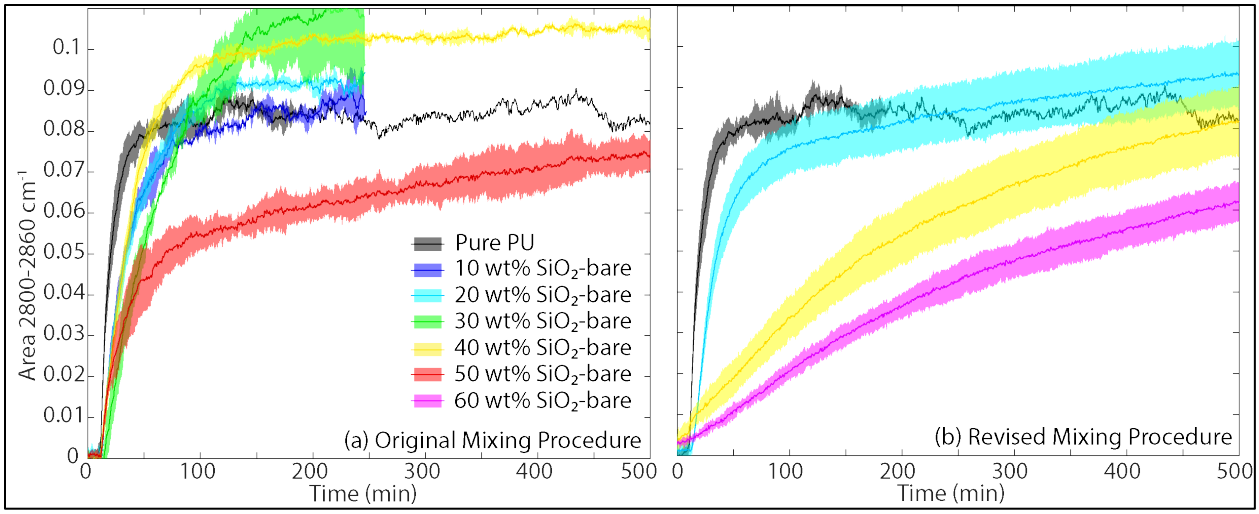


Figure 9. MeOH breakthrough in PU-unfunctionalized silica composites prepared with (a) original mixing protocol and (b) revised mixing protocol with different silica loadings: 0 wt% (black), 10 wt% (blue), 20 wt% (cyan), 30 wt% (green), 40 wt% (yellow), 50 wt% (red), and 60 wt% (magenta). Shaded regions bounding the breakthrough curves indicate the standard deviation over multiple runs (typically three runs per condition).

The swelling of the polymer matrix upon uptake of penetrant can be characterized by a normalized change in volume or strain ($\varepsilon$). The change in volume can also be written in terms of a change in density (or mass concentration):

$$\varepsilon(t) = \frac{V(t) - V_0}{V_0} = \frac{\rho_{\text{pol}}(t=0)}{\rho_{\text{pol}}(t)} - 1 \tag{4}$$

Assuming that the Beer–Lambert law applies, the IR absorbance of the polymer peak at 1230 $\text{cm}^{-1}$ is linearly proportional to the peak intensity or area, which is found by integrating the peak from $\nu_1$ = 1220 $\text{cm}^{-1}$ to $\nu_2$ = 1240 $\text{cm}^{-1}$:

$$\varepsilon(t) = \frac{\text{Area}_{\text{pol}}(t=0)}{\text{Area}_{\text{pol}}(t)} - 1 \tag{5}$$

Figure 10 compares the strain in the PU matrix determined from eq 5 for composites prepared with unfunctionalized $SiO_2$ using the original and revised mixing procedures. The composites prepared with the original mixing procedure quickly approached an equilibrium strain value between 0.00 and 0.01 for all loadings, whereas the composites prepared using the revised mixing procedure tended toward $\varepsilon$ of ~0.02 at equilibrium.

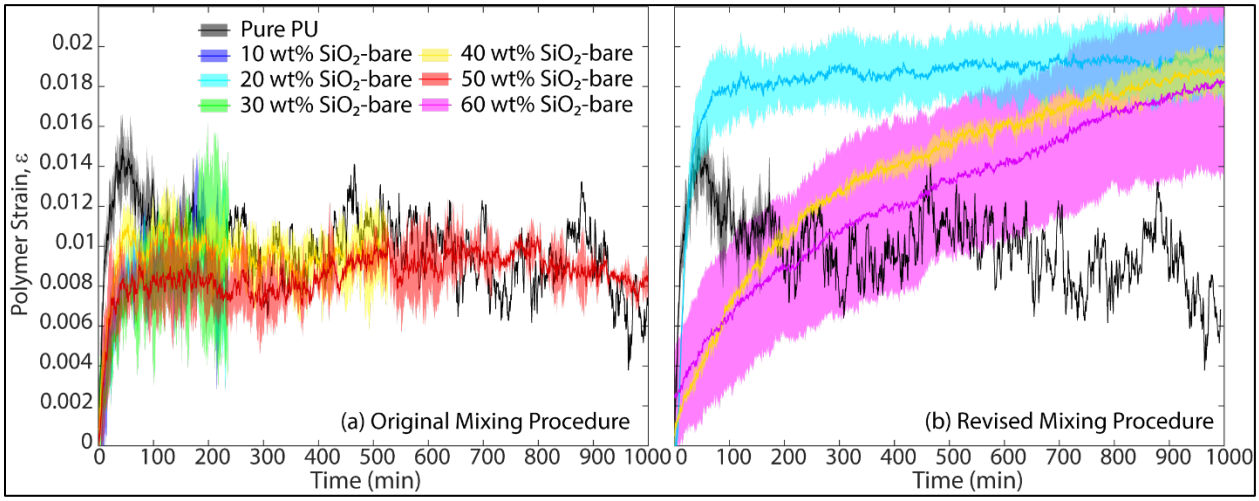


Figure 10. Polymer strain during MeOH breakthrough in PU-unfunctionalized silica composites prepared with (a) original mixing protocol and (b) revised mixing protocol with different silica loadings: 0 wt% (black), 10 wt% (blue), 20 wt% (cyan), 30 wt% (green), 40 wt% (yellow), 50 wt% (red), and 60 wt% (magenta).

The breakthrough curves in pure PU were used to fit to a Fickian diffusion model with constant diffusivity ($D$) as

$$\frac{\partial \tilde{c}}{\partial t} = D\frac{\partial^2 \tilde{c}}{\partial z^2} \tag{6}$$

The experimentally measured peak area for MeOH in the wavenumber range 2800–2860 $cm^{-1}$ is normalized to its equilibrium value ($Area_{MeOH,eq}$ = 0.084). Because concentration is proportional to the peak area according to the Beer–Lambert law, the normalized peak area is equivalent to the normalized MeOH concentration at the PU–ATR interface. The model-predicted concentration at the PU–ATR interface, $\tilde{c}\,(z = 0, t)$, is corrected to account for the penetration depth ($d_p$) of the evanescent wave from the ATR crystal into the PU film, according to

$$\tilde{c}_{\text{int}}(t) = \frac{\int_0^L \tilde{c}(z=0,t)\exp\left(-\frac{2z}{\mathrm{d}_p}\right)\mathrm{d}z}{\int_0^L \exp\left(-\frac{2z}{\mathrm{d}_p}\right)\mathrm{d}z} \tag{7}$$

The penetration depth of the evanescent wave in the ATR crystal is given as

$$d_p = \frac{\lambda}{2\pi n_{\text{ATR}}\sqrt{\sin^2\theta - {}^{n_p}/_{n_{\text{ATR}}}}} \tag{8}$$

where λ is the wavelength of the IR light; $n_{\text{ATR}}$ and $n_p$ are the refractive indices of the Ge ATR crystal and the polymer, respectively; and θ is the angle of incidence of the IR light at the polymer interface. For all cases in this work, $n_{\text{ATR}}$ = 4, $n_p$ = 1.5, and θ = 60°. This correction for the model prediction is important for thinner films ($L < 10d_p$).

The fit of diffusivity is carried out using the Levenberg–Marquardt nonlinear least-squares algorithm as implemented in the MATLAB function nlinfit, which minimizes the sum-of-square errors between the model-predicted interface concentration ($\tilde{c}_{\mathrm{int}}(t)$) and the experimentally measured normalized MeOH peak area from 2800 to 2860 $cm^{-1}$, $Area_{MeOH}/Area_{MeOH,eq}$. The fitting procedure yielded a value of $D = 4.7 \times 10^{-14}$ $m^2/s$, as shown in Figure 11 (a), along with plots of the experimental and best-fit model normalized breakthrough curves.

Assuming the composites behaved ideally, or in other words, if MeOH permeated the PU matrix with the same diffusivity with the $SiO_2$ particles acting as impermeable obstructions, the breakthrough dynamics could be predicted by the Maxwell model,[44] which gives the effective solubility ($S$) and diffusivity ($D$) of a penetrant in terms of their values in the pure polymer ($S_0$ and $D_0$, respectively) and the volume fraction of solid in the composite ($\phi_d$):

$$\frac{S}{S_0} = 1 - \phi_d, \qquad \frac{D}{D_0} = \frac{1}{1 + 0.5\phi_d} \tag{9}$$

Using the values predicted by eq 9 along with the measured thicknesses of the PU–$SiO_2$ composites summarized in Table 1, the breakthrough curves were simulated and compared to those obtained experimentally as shown in Figure 11 (b). It is shown that after an initial period, where the agreement between the Maxwell model and experimental breakthrough curves is reasonable, the experimental curves continue to increase, indicating additional MeOH uptake, whereas the model predicts that the system reaches equilibrium.

Table 1. Summary of Parameters Used to Simulate MeOH Breakthrough in PU–$SiO_2$ Composites Using the Maxwell Model

| Weight Fraction, $\omega_{SiO2}$ | Volume Fraction, $\phi_{SiO2}$ | $\frac{S}{S_0}$ | $\frac{D}{D_0}$ | Measured Film Thickness, $L$ (μm) |
|---|---|---|---|---|
| 0.20 | 0.12 | 0.88 | 0.94 | 13.3 |
| 0.39 | 0.26 | 0.74 | 0.89 | 22.0 |
| 0.58 | 0.43 | 0.57 | 0.82 | 29.0 |

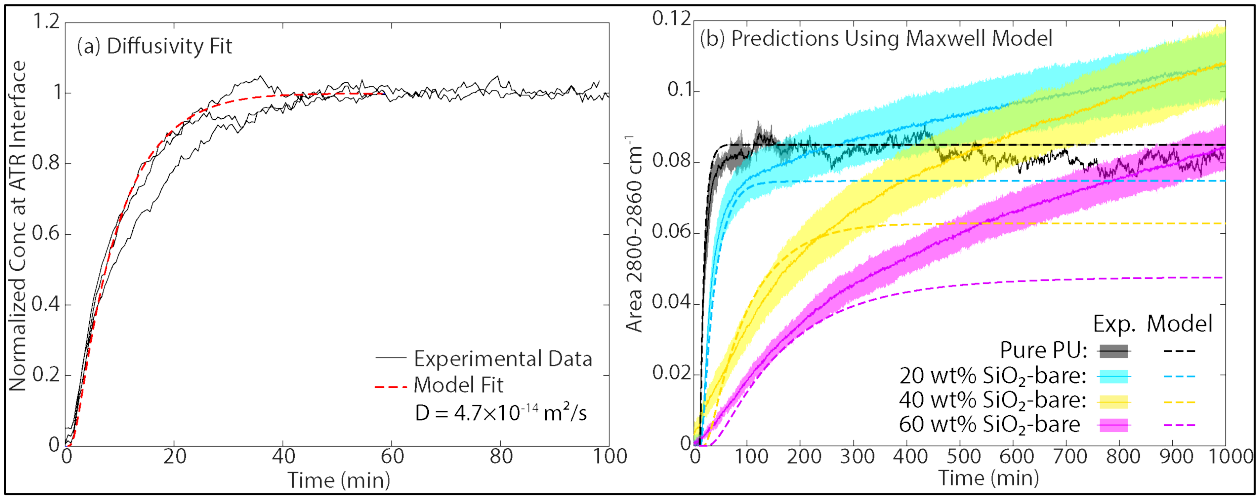


Figure 11. (a) Fit of Fickian diffusion model to MeOH breakthrough in pure PU showing normalized experimental peak area (black lines, three replicates); best-fit model prediction (dashed red line); and fit value of diffusivity ($D = 4.7 \times 10^{-14}$ m$^2$/s). (b) Experimental (solid lines) and model-predicted (dashed lines) breakthrough curves of MeOH in PU-unfunctionalized silica composites with 0 wt% (black), 20 wt% (cyan), 40 wt% (yellow), and 60 wt% (magenta) silica loading.

A possible explanation for the observed breakthrough curves is that the MeOH diffuses into or through two distinct regions in the composite: (1) the unperturbed bulk PU matrix and (2) interfacial regions surrounding the PU particles at a much slower rate but with a much higher equilibrium solubility as compared to the bulk PU. This behavior would be consistent with a rigidified polymer layer at the particle interface due to strong particle–polymer interaction coupled with a strong chemical affinity of the penetrant with the interfacial region. In this view, MeOH diffuses through the bulk PU matrix relatively quickly, then begins to slowly infiltrate the interfacial regions, adsorbing to the silica surface while slowly displacing PU chains from the surface of the silica particles so that MeOH accumulates there. To assess the feasibility of this interpretation, consider the potential contribution of MeOH bound to silica particles to the total observed IR intensity or peak area. According to Zhuravlev,[45] the surface density of silanol (Si–OH) sites on amorphous silica ($\alpha_{\mathrm{OH,sil}}$) is 4.6 nm$^{-2}$. Using the surface-area-to-volume ratio for a sphere ($3/R$) and the volume fraction of silica in the composite, an estimated volumetric concentration of silanol sites, and therefore, MeOH adsorbed, onto the silica surfaces in the composite ($c_{\mathrm{MeOH,ads}}$) can be estimated as

$$c_{\mathrm{MeOH,ads}} = \alpha_{\mathrm{OH,sil}} \frac{3\phi_{\mathrm{SiO_2}}}{N_{\mathrm{av}} R} \tag{10}$$

Including the nominal silica particle radius of 250 nm that is used in these studies yields a MeOH concentration of $9.17 \times 10^{-5} \phi_{\mathrm{SiO_2}}$ mol/cm$^3$ per layer of MeOH adsorbed. Previous work on the sorption of MeOH into the same pure PU using a quartz crystal microbalance showed that the equilibrium concentration of MeOH in the PU film when exposed to a MeOH vapor with activity 0.1 in $N_2$ was $2.2 \times 10^{-4}$ mol/cm$^3$. For a PU–$SiO_2$ film with $\phi_{\mathrm{SiO_2}}$ of 0.5, adsorption of 4–5 MeOH layers at the silica surface would be required to contribute an

equal amount to the IR signal as the MeOH absorbed in the bulk PU. Given the tendency of MeOH to H-bond with itself and form clusters, this seems within the realm of possibility.

It is also useful to examine the behavior of the IR spectra for MeOH for the different loading levels of silica in the PU-$SiO_2$ composites. Figure 12 shows the difference spectra obtained for the MeOH breakthrough experiments in the PU-unfunctionalized silica composites focused on the symmetric $CH_3$ stretching peak ($\nu_s(CH_3)$) for MeOH. It is shown that for the pure PU composite, $\nu_s(CH_3)$ is 2829 $cm^{-1}$ with no shift in peak position as the experiment proceeds. However, for the silica-loaded PU, there is clearly a blue shift of the MeOH $\nu_s(CH_3)$ peak as the experiment proceeds, and the blue shift increases for higher loadings. This behavior is supported by published studies that show that the $\nu_s(CH_3)$ band of MeOH increases from 2847 to 2858 $cm^{-1}$ when sorbed onto silica.[46] Similar analysis of the OH region was difficult due to the additional contributions from PU in this work.

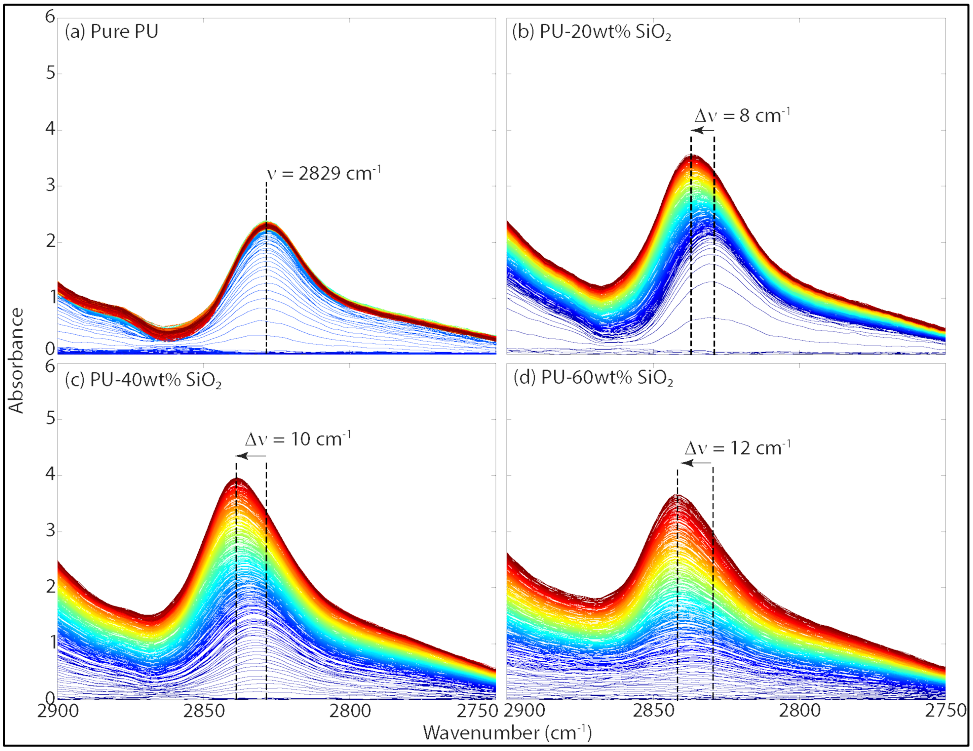


Figure 12. Difference spectra during breakthrough of MeOH in PU-unfunctionalized silica composites with different loading levels: (a) 0 wt%, (b) 20 wt%, (c) 40 wt%, and (d) 60 wt%. In all cases, the reference for the difference spectra was taken from the corresponding dry composite at the beginning of each experiment. Line colors indicate relative time from the beginning of the experiment; blue corresponds to early times and red to later times.

The breakthrough dynamics and polymer swelling are compared for different silica surface chemistries at each particle loading level in Figures 13, 14, and 15 for loading levels of 20, 40, and 60 wt%, respectively. An interesting behavior emerges for the 40 and 60 wt% loading cases for the amine-functionalized silica composites. In the first few hundred

minutes, the breakthrough curves were similar. They then went through an inflection, where the breakthrough rate appeared to increase dramatically before reaching an equilibrium, while the corresponding breakthrough curves for the unfunctionalized silica composites increased at a constant rate for the entire experiment. Assuming that MeOH sorption on the surface of the silica particles explains the deviation from Maxwell behavior in both cases, this indicates that the MeOH accumulated on the amine-functionalized silica particles faster than on the unfunctionalized silica particles. The cause of this difference is not clear, but one possible explanation is that the PU chains were less tightly bound and/or less dense at the surface of the amine-functionalized silica particles, so that the PU chains were more easily displaced by adsorbing MeOH molecules.

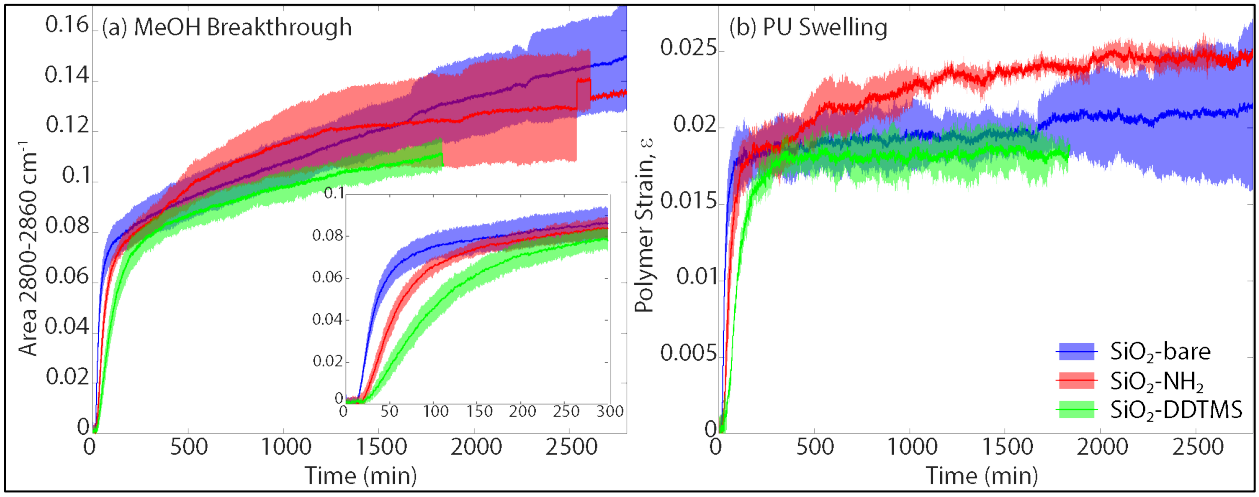


Figure 13. (a) MeOH breakthrough dynamics and (b) polymer swelling for 20 wt% silica–PU composites made with unfunctionalized (blue), amine-functionalized (red), and dodecyltrimethoxysilane (DDTMS)-functionalized (green) silica particles.

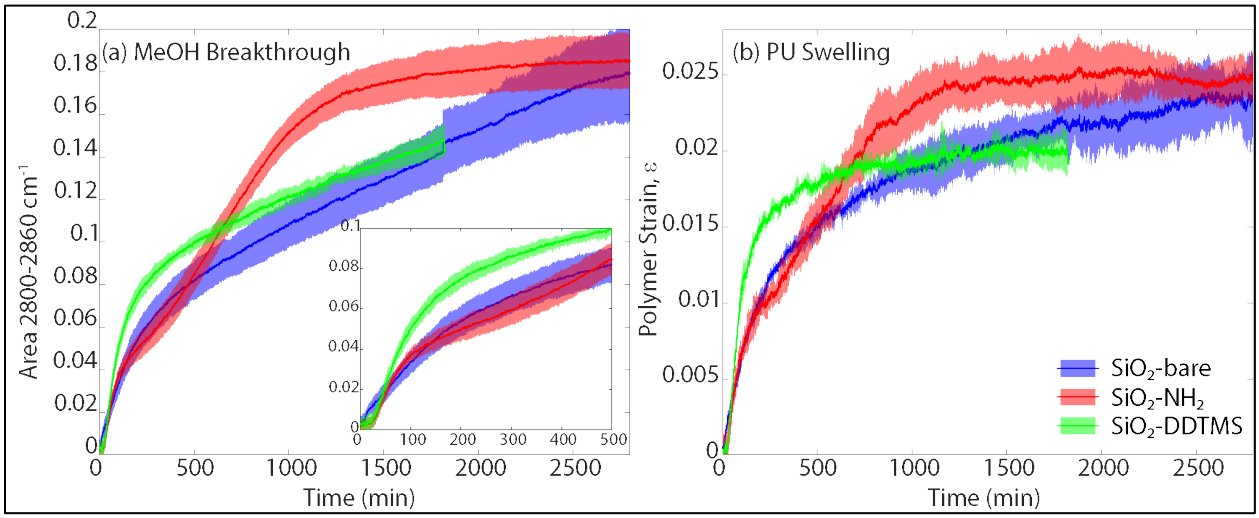


Figure 14. (a) MeOH breakthrough dynamics and (b) polymer swelling for 40 wt% silica–PU composites made with unfunctionalized (blue), amine-functionalized (red), and DDTMS-functionalized (green) silica particles.

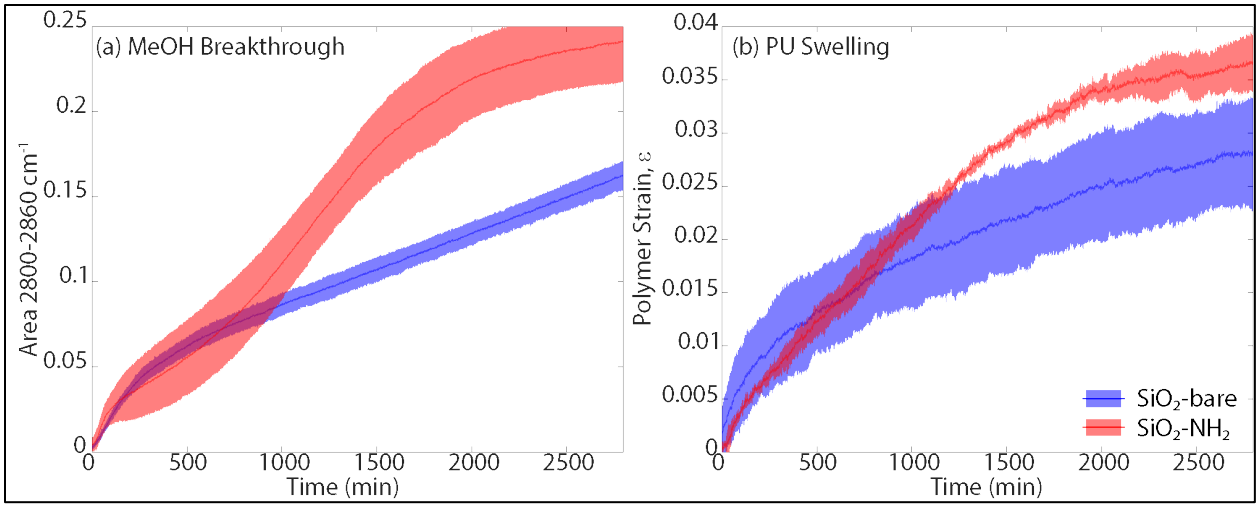


Figure 15. (a) MeOH breakthrough dynamics and (b) polymer swelling for 60 wt% silica–PU composites made with unfunctionalized (blue) and amine-functionalized (red) silica particles.

### 3.3 Colloidal Force Spectroscopy

Colloidal probes were examined via optical microscopy before each experiment to ensure that each probe was suitable. Figure 16 (a) and (b) shows examples of a "good" probe, in which the light reflection from the silica particle is clear (i.e., the reflective silica is not covered in adhesive and is attached at the end of the cantilever). An example of a "bad" probe is shown in Figure 16 (c) and (d), in which the silica particle is encapsulated by the adhesive, changing the particle's appearance in the microscope images; additionally, the particle is not located at the tip of the cantilever. Probes were also checked periodically throughout a given experiment and at the end of each experiment to ensure that the silica particle was not compromised.

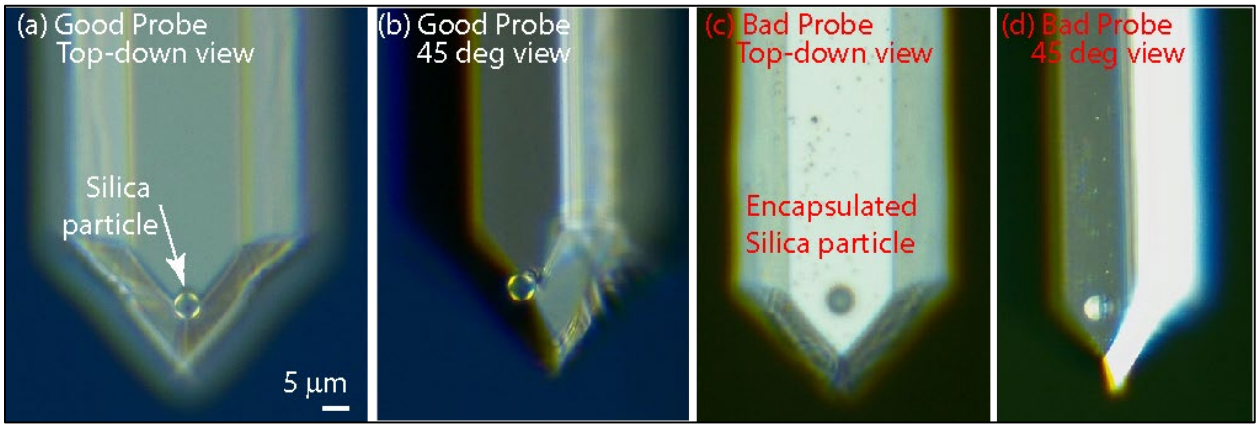


Figure 16. Optical microscope images of colloidal probes made with 5 µm silica particles: (a) successful attachment, top view; (b) 45° view and unsuccessful attachment; (c) top view; and (d) 45° view.

Results of colloidal force spectroscopy experiments over several different probes for each silica surface chemistry are shown in Figure 17 (unfunctionalized), Figure 18 (amine functionalized), Figure 19 (dodecyltrimethoxysilane [DDTMS] functionalized), and Figure 20 (carboxyl functionalized). In each experiment, a force curve was acquired at each point on an equally spaced 5 × 5 grid covering a 100 μm × 100 μm area of a PU sample using a maximum indentation force ($F_{\text{ind}}$) of 0.5 μN. This was performed from 40 to 90 °C in 10 °C increments for each probe, allowing the system to reach thermal equilibrium between each run (approximately 15 min). For each force curve, the indentation into the sample (δ) is determined from the approach portion of the curve as the difference between the point of contact ($z_c$) and the maximum $z$ position ($z_{\text{max}}$) minus the cantilever deflection (Δ):

$$\delta = (z_{\text{max}} - z_c) - \Delta \tag{11}$$

The adhesion force ($F_{\text{adh}}$) was determined as the minimum point on the retraction portion of the force curve. The Johnson–Kendall–Roberts (JKR) contact mechanics model was used to compute the contact radius ($a$), the reduced modulus ($E^*$), the spherical indenter radius ($R$), and the specific surface energy of the particle–polymer interaction (γ) from the following equations:

$$F_{\text{adh}} = \frac{3\pi R\gamma}{2} \tag{12}$$

$$\delta = \frac{a^2}{R} - \frac{2}{3}\sqrt{\frac{9(1-\nu^2)\pi a\gamma}{2E^*}} \tag{13}$$

$$a^3 = \frac{R}{E^*}\left(F_{\text{ind}} + 3\pi R\gamma + \sqrt{6\pi R\gamma F_{\text{ind}} + (3\pi R\gamma)^2}\right) \tag{14}$$

The adhesion work ($W_{\text{adh}}$) was also computed from the area under the retraction portion of the force curve from the between-the-contact point and the pull-off point:

$$W_{\text{adh}} = \int_{z_c}^{-\infty} F_{\text{ret}}(z)\mathrm{d}z \tag{15}$$

For all surface chemistries, the JKR model predicted the PU modulus to be on the order of 1 GPa for temperature of 40–60 °C, which aligns with expectations.[47] Between 60 and 70 °C, there was an ~2 order of magnitude decrease in the modulus, indicating that the $T_g$ of the PU was in this temperature range. This aligns with the $T_g$ of 65 °C that was determined in previous work using DSC.[17] Concurrent with the decrease in modulus, there were increases in the indentation (δ), contact radius ($a$), specific surface energy (γ), and work of adhesion ($W_{\text{adh}}$) between 60 and 70 °C.

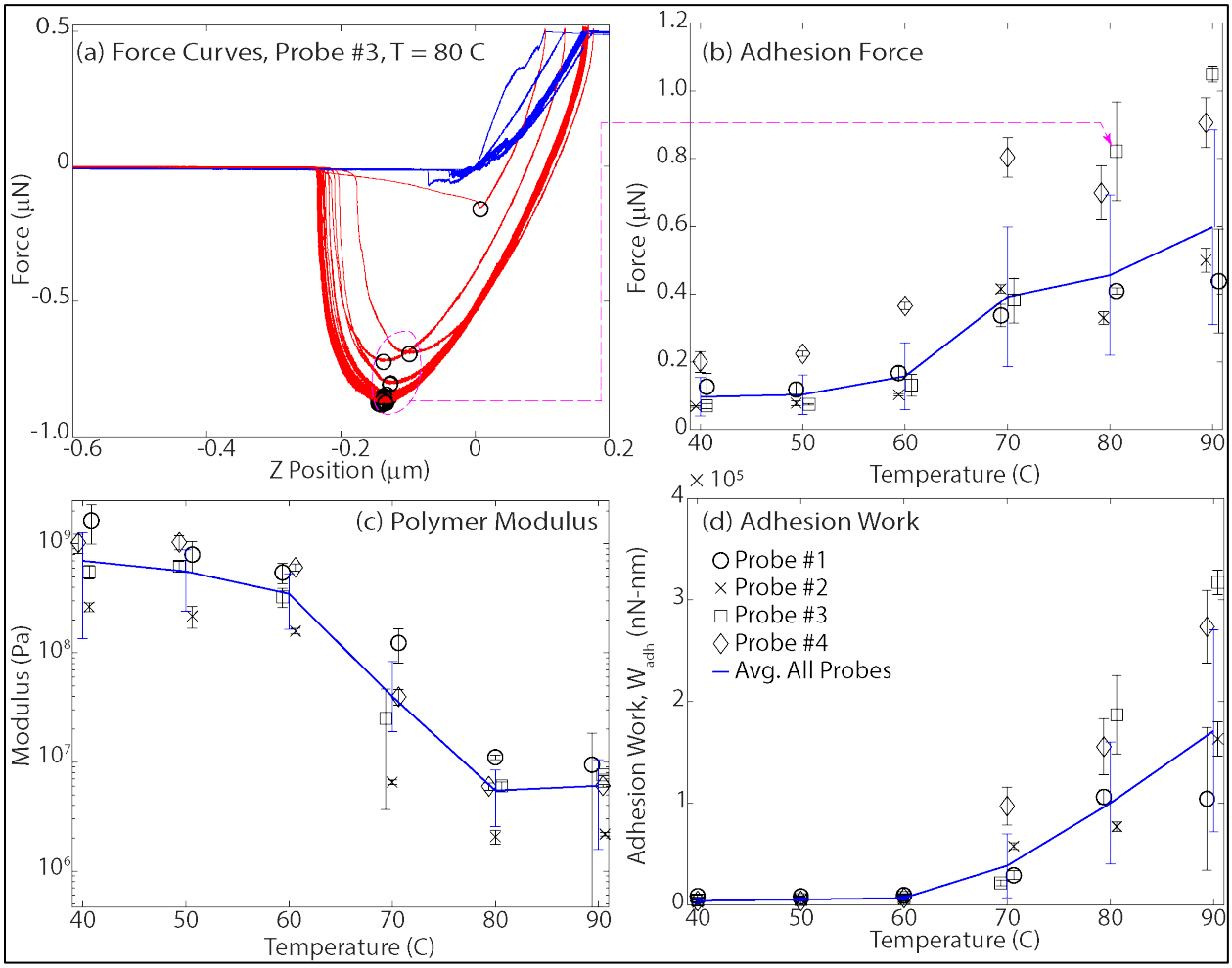


Figure 17. Colloidal force spectroscopy results for 5 μm diameter unfunctionalized silica probes on PU. (a) Force curves obtained with probe 3 at 80 °C on a 5 × 5 (100 μm × 100 μm) grid. Approach, blue curves; retract, red curves; adhesion force, black circles. (b) Adhesion force. (c) Modulus. (d) Adhesion work as a function of temperature for probes 1 (circles), 2 (x's), 3 (squares), and 4 (diamonds) and average over all probes (blue lines). Some data points were shifted slightly along the *x* axis to avoid overlap and clarify the presentation.

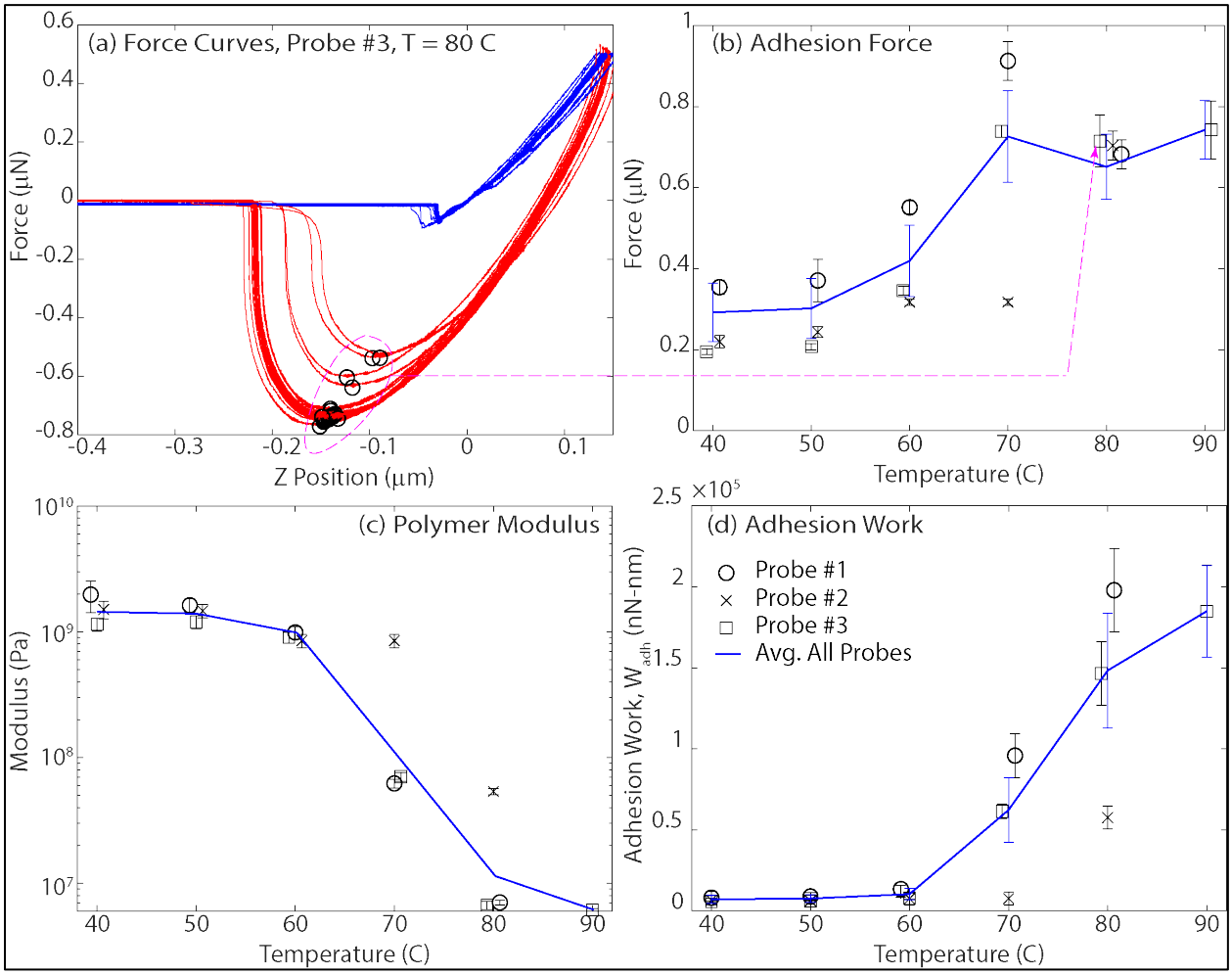


Figure 18. Colloidal force spectroscopy results for 5 µm diameter amine-functionalized silica probes on PU. (a) Force curves obtained with probe 3 at 80 °C on a 5 × 5 (100 µm × 100 µm) grid. Approach, blue curves; retract, red curves; adhesion force, black circles. (b) Adhesion force. (c) Modulus. (d) Adhesion work as a function of temperature for probes 1 (circles), 2 (x's), 3 (squares), and average over all probes (blue lines). Some data points were shifted slightly along the *x* axis to avoid overlap and clarify the presentation.

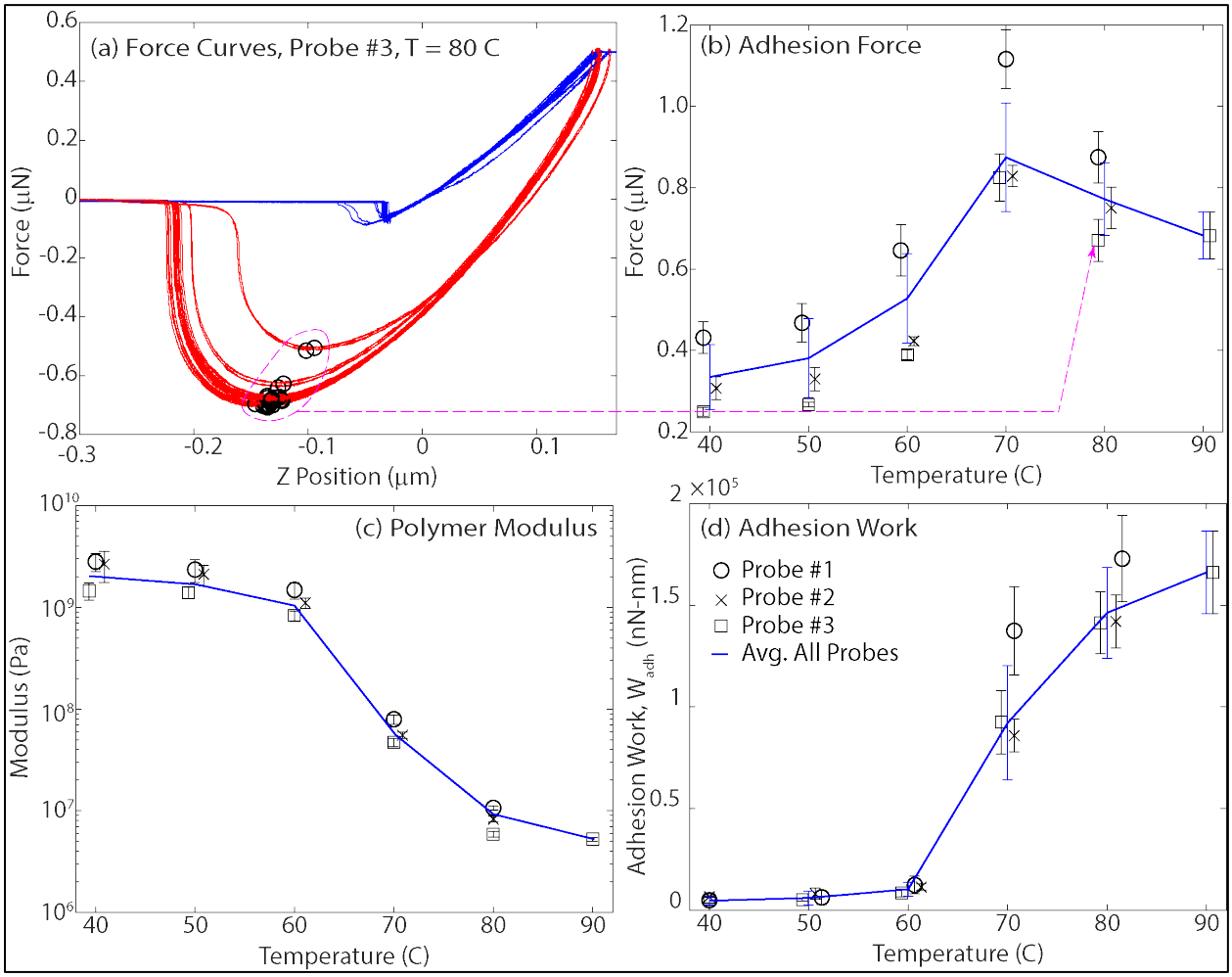


Figure 19. Colloidal force spectroscopy results for 5 μm diameter DDTMS-functionalized silica probes on PU. (a) Force curves obtained with probe 3 at 80 °C on a 5 × 5 (100 μm × 100 μm) grid. Approach, blue curves; retract, red curves; adhesion force, black circles. (b) Adhesion force. (c) Modulus. (d) Adhesion work as a function of temperature for probes 1 (circles), 2 (x's), 3 (squares), and average over all probes (blue lines). Some data points were shifted slightly along the *x* axis to avoid overlap and clarify the presentation.

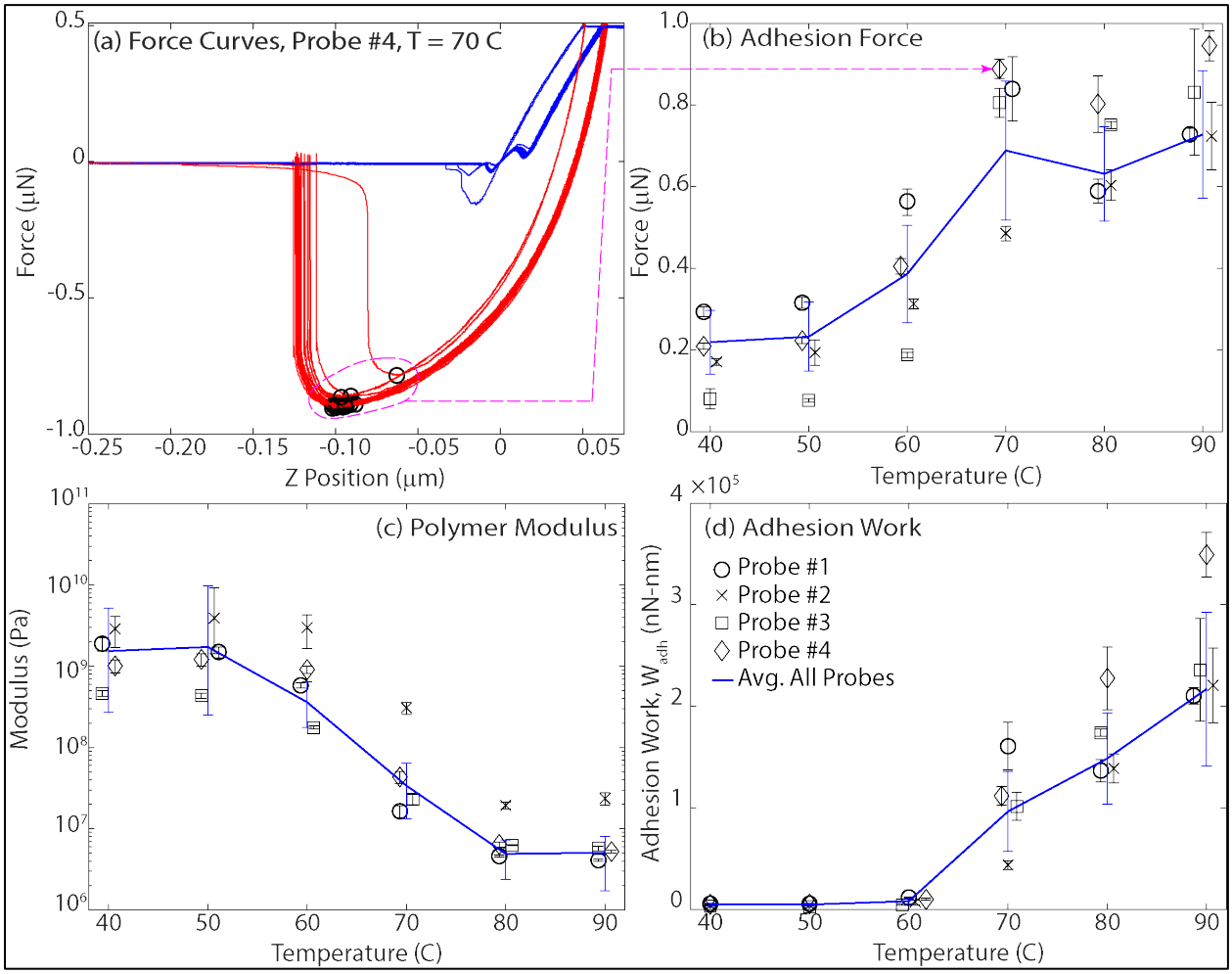


Figure 20. Colloidal force spectroscopy results for 5 μm diameter carboxyl-functionalized silica probes on PU. (a) Force curves obtained with probe 3 at 70 °C on a 5 × 5 (100 μm × 100 μm) grid. Approach, blue curves; retract, red curves; adhesion force, black circles. (b) Adhesion force. (c) Modulus. (d) Adhesion work as a function of temperature for probes 1 (circles), 2 (x's), 3 (squares), 4 (diamonds), and average over all probes (blue lines). Some data points were shifted slightly along the *x* axis to avoid overlap and clarify the presentation.

Figure 21 shows the adhesion work and specific surface energy on the same plots for comparison across all of the silica surface chemistries on PU. Below the $T_g$, the polymer chains cannot rearrange themselves sufficiently fast to form an equilibrium interface with the silica surface. Thus, the adhesion work and specific surface energy are not good indicators of particle–polymer interaction strength below 65 °C in this case. Above this temperature, the polymer chains are free to rearrange themselves and optimize their interaction with the silica surface so that the adhesion work and specific surface energy are better indicators of the particle–polymer interface as it exists in corresponding composite films. Taking the values at a temperature of 80 °C, the specific surface energy computed from the JKR model appears to be lowest for the unfunctionalized silica, approximately the same for amine- and carboxyl-functionalized silica, and slightly higher for the DDTMS-functionalized silica. The result for

the $SiO_2$–DDTMS particle is particularly surprising because the aliphatic hydrocarbon chains should not form H-bonds with the PU chains, and thus should interact to a lesser degree than a silica surface covered with $NH_2$ or COOH groups.

There do not appear to be any clear correlations between the PU–silica specific surface energy and breakthrough dynamics of MeOH in PU–silica composites. As noted in Section 3.2, the early-time breakthrough dynamics appear to be driven by MeOH diffusion in the polymer, and at later times, the dynamics appear to be driven by MeOH accumulation at the silica surface. Based on this, it is expected that the later time dynamics would be inversely proportional to the PU–silica specific surface energy (i.e., it is harder for MeOH to displace more strongly bound PU from the silica surface). However, the MeOH breakthrough dynamics were observed to be faster for the amine-functionalized silica than the unfunctionalized silica. The fact that the silica particles used for the colloidal probes were processed in a different manner than those used in composite film preparation makes it difficult to confidently link the specific surface energies determined from the colloidal force spectroscopy experiments to chemical breakthrough experiments. In future work, closer attention should be given to the silica surface preparation, to ensure that it is identical across all experiments.

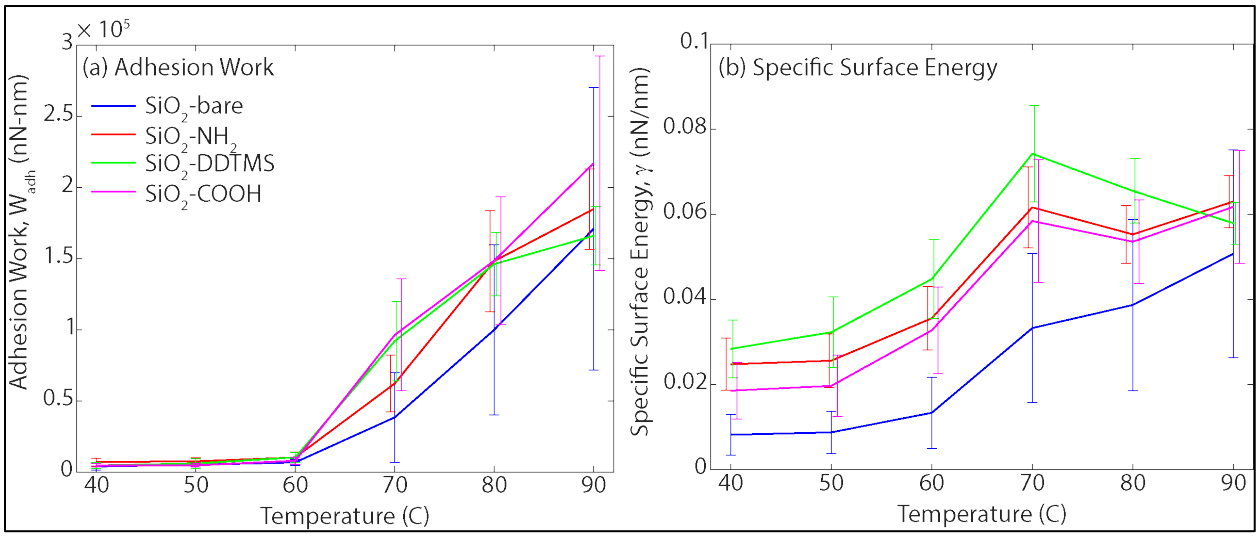


Figure 21. (a) Adhesion work and (b) specific surface energy over all probes for each silica surface chemistry. Blue, unfunctionalized; red, amine; green, DDTMS; and magenta, carboxyl.

## 3.4 AFM Imaging of Composite Cross Sections

The primary goal of the AFM imaging was to determine whether an interfacial layer of polymer was present at the particle interface that had properties different from those of the bulk polymer.

### 3.4.1 AM–FM Imaging

Images of a cross-sectioned PU–$SiO_2$ bare composite obtained with AM–FM AFM are shown in Figure 22. In addition to the topography ($z$; Figure 22 (a)) and phase ($\phi$; Figure 22 (b)) obtained from the first mode as in standard AM–AFM (tapping mode), there were two additional channels related to the second mode. As the probe scanned over the surface, the frequency of the second mode was adjusted to maintain a phase of 90°, providing the frequency shift ($\Delta f_2$) that indicated stiffness and elasticity (Figure 22 (c)), while the input voltage was adjusted to maintain a constant second-mode oscillation amplitude of the cantilever, providing the dissipation ($V_2$; Figure 22 (d)). The topography shows that the particles were successfully sectioned: an ~10 nm height variation is displayed between the particle and the surrounding polymer matrix. Ideally, the topography would be flat, so that there are no abrupt height changes at the particle–polymer interface that would introduce measurement artifacts and thereby prevent the accurate determination of polymer properties at the interface relative to the bulk. This issue is addressed in more detail below. The phase provides information on variation of material properties and tip-sample interaction. The phase can be related as a loss tangent (tan δ), which is equivalent to that of the material in the absence of surface effects such as capillary bridging between the tip and sample and squeeze film damping:[48,49]

$$\tan\delta = \frac{\frac{A_1}{A_{1,\text{free}}} - \sin\phi}{\cos\phi} \tag{16}$$

where $A_{1,\text{free}}$ is the oscillation amplitude of the cantilever in the first mode, far away from the material surface (nm or V), and $A_1$ is the oscillation amplitude of the cantilever in the first mode while imaging (nm or V).

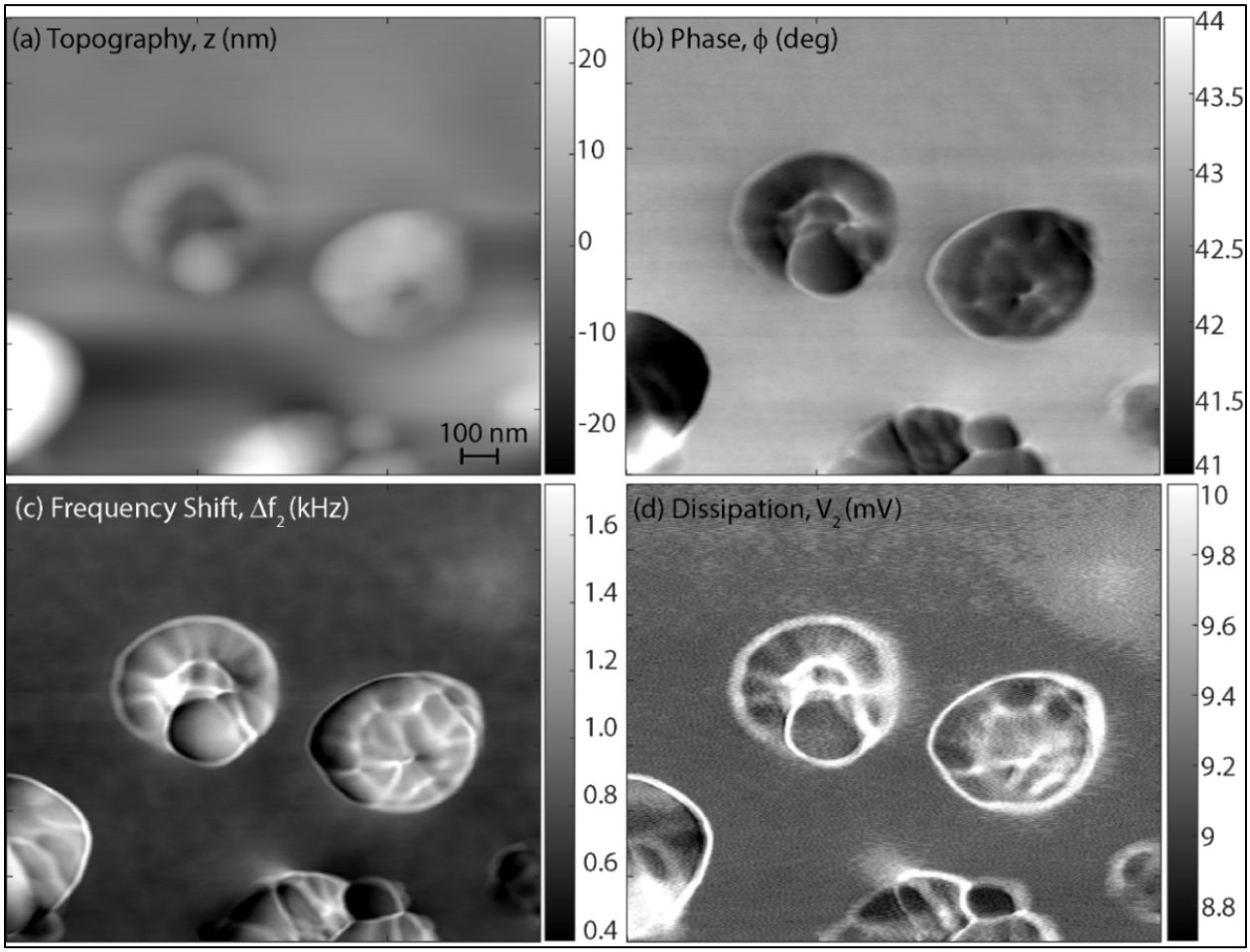


Figure 22. Cross-sectioned PU-unfunctionalized silica composites obtained with AM–FM AFM: (a) topography, (b) phase contrast, (c) second-mode frequency shift, and (d) second-mode dissipation.

The frequency shift ($\Delta f_2$) provides information on material stiffness: higher values indicate higher stiffness. Dissipation is related to energy losses including within the material (viscoelastic) but also from other sources, such as capillary bridging and squeeze film damping. As expected, Figure 22 shows that the cross-sectioned silica particles are stiffer than the surrounding polymer matrix. The AFM outputs can also be related to material properties such as the reduced modulus ($E_R$), which represents elastic deformation that occurs in the material and the tip:[50–52]

$$E_R = \frac{4\sqrt{2}}{\sqrt{R}} Q_1 k_1 \left(\frac{k_2}{k_1}\frac{\Delta f_2}{f_{2,0}}\right)^2 \frac{A_1^{3/2}}{A_{1,\text{free}}^2 - A_1^2} \tag{17}$$

where $R$ is the radius of the AFM tip in contact with the material surface (m), $k_i$ is the spring constant of the cantilever in the $i$th mode (N/m), $Q_i$ is the quality factor of the $i$th mode; and $f_{2.0}$ is the frequency of the second mode far away from the surface (Hz).

$E_R$ is related to the modulus of the material ($E_{\text{mat}}$) and AFM tip ($E_{\text{tip}}$) by

$$\frac{1}{E_R} = \frac{1-\nu_{\text{mat}}^2}{E_{\text{mat}}} + \frac{1-\nu_{\text{tip}}^2}{E_{\text{tip}}} \tag{18}$$

where $\nu_i$ is Poisson's ratio of component *i*, indicating compressibility.

The compressive viscosity of the material ($\eta_c$) is related to the dissipated energy ($E_{\text{dis}}$), the virial ($V_1$), and reduced modulus ($E_R$):[50]

$$\eta_c = \frac{1}{(2\pi)^2 f_1}\frac{E_{\text{dis}}E_R}{V_1} \tag{19}$$

$$E_{\text{dis}} = \frac{\pi k_1 A_1}{Q_1}\left(A_{1,\text{free}}\sin\phi - A_1\right) \tag{20}$$

$$V_1 = \frac{k_1 A_{1,\text{free}}}{2Q_1} A_1 \cos\phi \tag{21}$$

The indentation ($\delta$) of the AFM tip into the sample can be computed by

$$\delta = \frac{1}{2Q_1}\frac{k_1}{k_2}\frac{f_{2,0}}{\Delta f_2}\left(A_{1,\text{free}}^2 - A_1^2\right)^{1/2} \tag{22}$$

The topography map can be corrected by accounting for the indentation as $z_{\text{corr}} = z + \delta$.

Figure 23 displays the computed values of (a) loss tangent (tan $\delta$), (b) reduced modulus ($E_R$), and compressive viscosity ($\eta_c$), (c) tip indentation ($\delta$), and (d) corrected topography ($z_{\text{corr}}$) with an assumed tip radius of 5 nm. As expected, tan $\delta$, $E_R$, and $\eta_c$ are all higher for the cross-sectioned silica particle than for the surrounding polymer matrix. The $E_R$ value of ~0.5 GPa in the bulk polymer also aligns well with the modulus determined by colloidal force spectroscopy and DMA ($E$ of ~1 GPa). The indentation in the polymer matrix was 9–10 nm, and the resulting corrected topography shows a step change in the height between 0 and 6 nm, depending on the specific location along the interface of each particle.

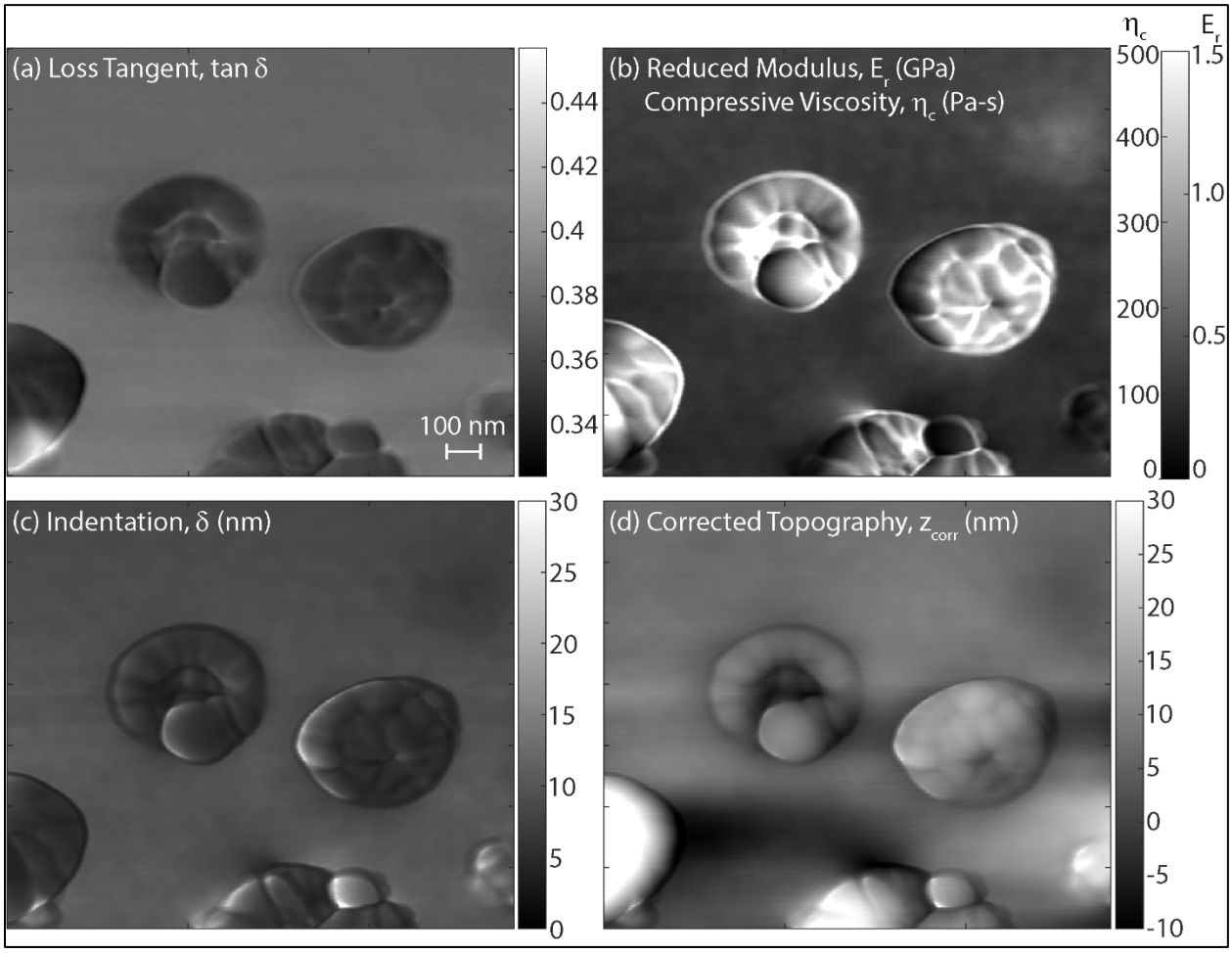


Figure 23. Computed quantities from AM–FM images of cross-sectioned PU-unfunctionalized silica composites: (a) loss tangent, (b) reduced modulus and compressive viscosity, (c) tip indentation into material, and (d) corrected topography.

The $E_R$ and $\eta_c$ images also show an apparent interfacial region with higher values at the particle interface as compared with the bulk polymer matrix. To determine the extent of the observed interfacial region, two methods were used. In the first method, the boundary of one of the particles (the lefthand one in Figures 22 and 23) was manually drawn using MATLAB's drawpolygon function. This boundary was then offset 50 pixels inward, and the values tan δ, $E_R$, and $\eta_c$ were plotted as a function of normal distance from the boundary, averaging the values in 2.5 nm bins as shown on the left side of Figure 24. Data for the left and right sides of the particle are presented separately to assess potential scan-direction effects in the data. It is shown that the tan δ curve transitions between two approximately constant values (0.362 to 0.376) over a 30 nm interval; this can be used to define the interfacial region. Plotting histograms of the data shows that tan δ was lower in the interfacial region, while $E_R$, and $\eta_c$ were both higher in the interfacial region as compared to the bulk. Additionally, the distributions were significantly wider in the interfacial region as compared to the bulk.

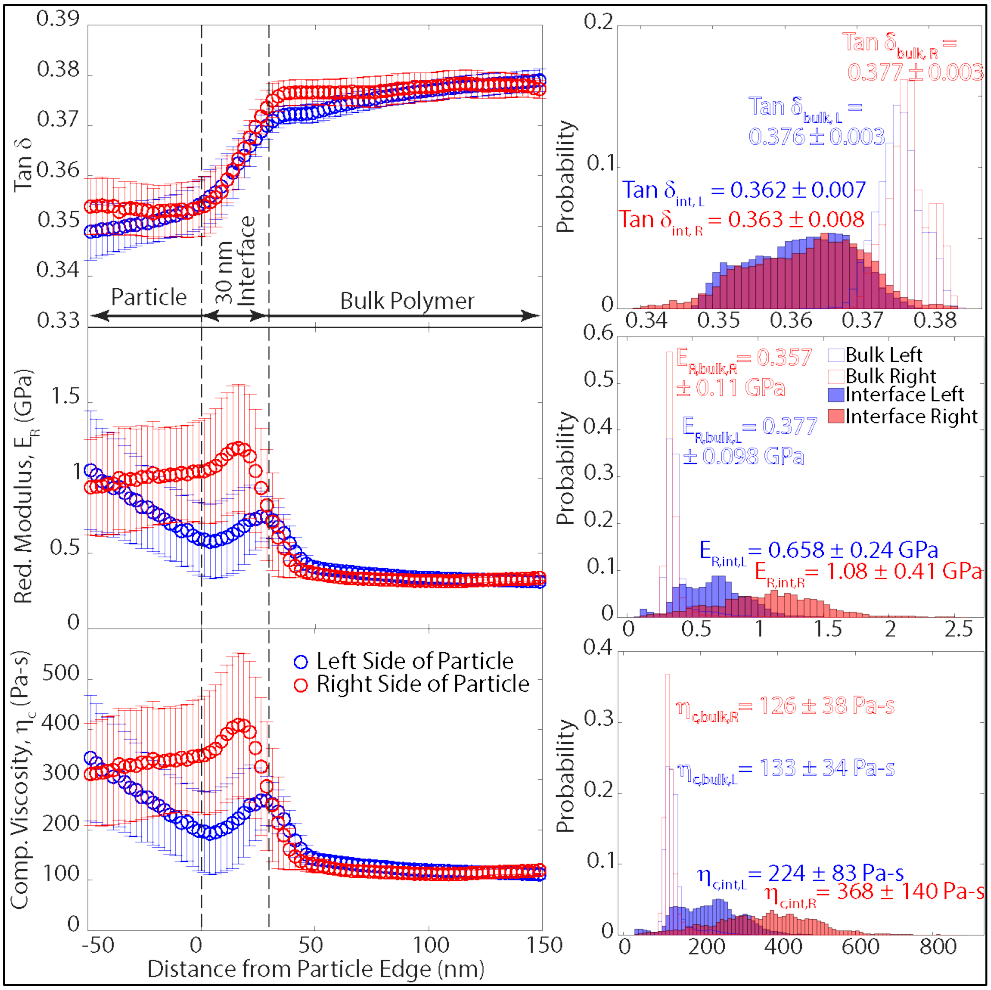


Figure 24. Plots of tan δ (top left), $E_R$ (middle left), and $\eta_c$ (bottom left) as a function of distance from the particle surface with data from left side (blue) and right side (red) of particle separated. Corresponding histograms for data within the interface region (unfilled bars) and bulk polymer (filled bars) are shown at right.

The second method used to assess the presence of an interfacial region was to plot the mechanical properties along lines extending across the interface from the particle to the bulk polymer. In Figure 25 (b)–(d), the values of tan δ, $E_R$, and $\eta_c$ are plotted along the lines defined by the colored arrows superimposed on a map of tan δ in Figure 25 (a). In each of the plots, the particle edge was defined as the initial inflection point of the tan δ curve moving from the particle into the bulk polymer. The profiles are similar to those presented in Figure 24 in that the values of all the mechanical properties display a constant value with relatively little variance in the bulk polymer region, but have a much higher variance in the interfacial and bulk regions. The line profiles of $E_R$ and $\eta_c$ on the right side of the particle display a larger peak in the interfacial region as compared to the line profiles on the left side, which matches the results in Figure 24. This difference could arise from uneven cross sectioning of the particle or asymmetries in the tip geometry, which changes how the AFM tip interacts with the material surface near the interface. This is discussed in more detail below.

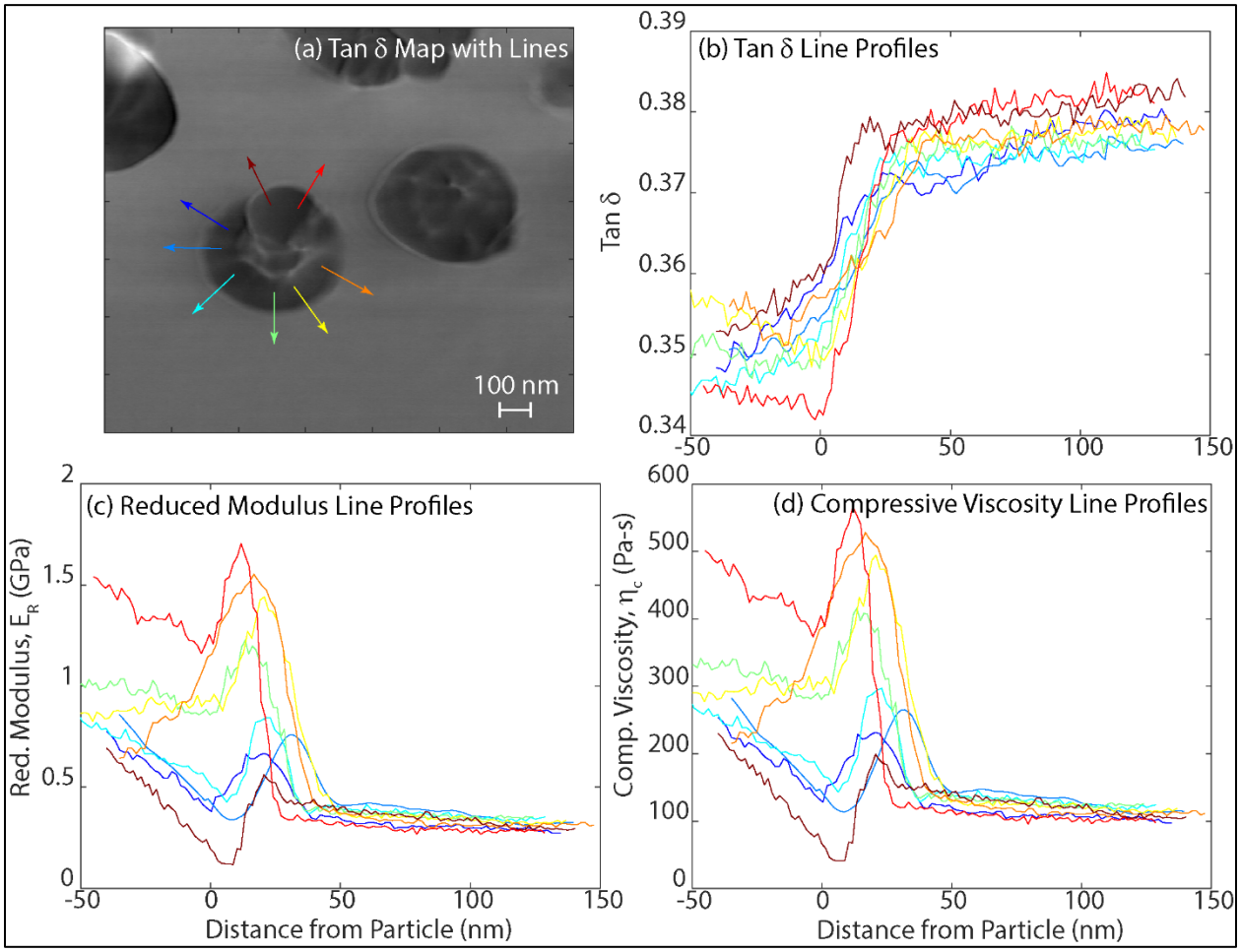


Figure 25. (a) Image of tan δ computed from AFM scan of cross-sectioned PU-unfunctionalized silica composite showing lines along which profiles are plotted (colored arrows). Profiles along each colored line are shown for (b) tan δ, (c) $E_R$, and (d) $\eta_c$. Arrow colors in (a) correspond to line colors in (b)–(d).

The tip-sample interaction near the particle interface must be properly accounted for to ensure that the mechanical properties are accurately determined. Specifically, considering step changes in the topography and the finite size of the tip, the tip can be simultaneously interacting with both the polymer and the particle, as shown in Figure 26. The sidewall of the tip interacts with the particle at increasing distances between the true particle–polymer interface and the centerline of the AFM tip as the indentation increases (Figure 26 (a)) and height differences between the polymer and particle increase (Figure 26 (b)). To minimize this effect, the indentation should be made as small as possible (~1 to 2 nm), and the cross section should be as flat as possible.[51,52] Certainly the indentation of ~10 nm and height difference of ~4 nm for the results shown in Figures 23–25 are not ideal, but for a given situation, determination of the minimum AFM tip-interface difference at which simultaneous interaction with both material phases occurs depends on the exact tip shape. For AFM tip-interface distances less than this critical value, the AFM outputs will contain contributions from both material phases. It is also worth noting that asymmetries in the tip geometry could influence the characterization of the

interface because different parts of the tip interact with the interface, depending on whether it is leading or trailing the scan direction. Therefore, good characterization of the tip geometry is necessary for interpreting the results (for example, using a calibration grating).

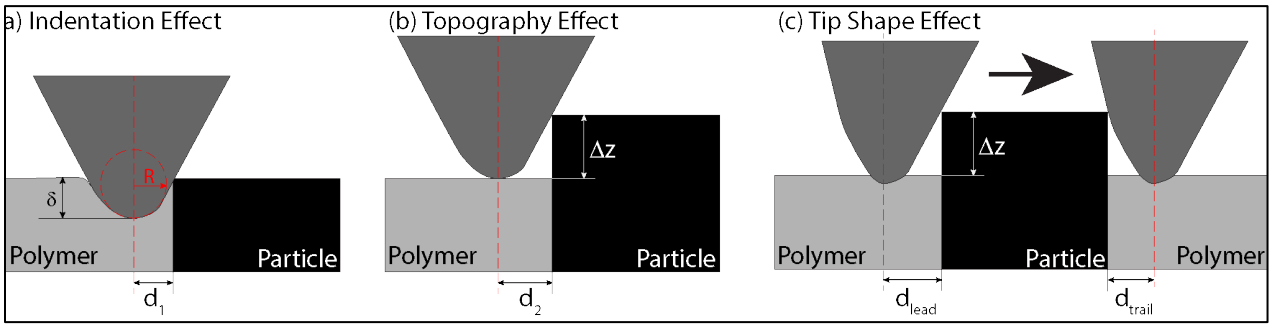


Figure 26. Influence of the AFM tip size and shape when imaging at a material interface: (a) effect of indentation, and (b) effect of step changes in topography.

Unfortunately, most of the particles in the cross-sectioned composites exhibited a substantial step change in topography at the particle interface. However, there were some particles that were sectioned nicely, at least along a portion of their boundary. Figure 27 (a) shows the topography image of a particle with small step change in height as compared to the surrounding polymer matrix. In Figure 27 (b)–(d), the values of tan δ, $E_R$, and $\eta_c$ are plotted along the lines defined by the colored arrows superimposed on a map of tan δ in Figure 25 (a). It is immediately apparent that the variation between the different line profiles is much less than in Figure 25. In addition to the smaller step change in topography at the particle interface, a cantilever with a lower spring constant ($k_1$ of 9 N/m compared to 36 N/m) and a lower free vibration amplitude ($V_{free}$ of 1 V compared to 2 V) was used, which led to a lower indentation (~1 nm compared to ~9 nm). Again, the interfacial region was defined as the distance over which the value of tan δ changed. In this case, the compressive viscosity ($\eta_c$) only changes within the interfacial region defined by tan δ and is constant outside. However, the reduced modulus ($E_R$) displays a spatial gradient for an additional 10–15 nm outside of this defined interfacial region into the bulk of the polymer matrix, which could be indicative of an interfacial region with higher modulus than the bulk polymer.

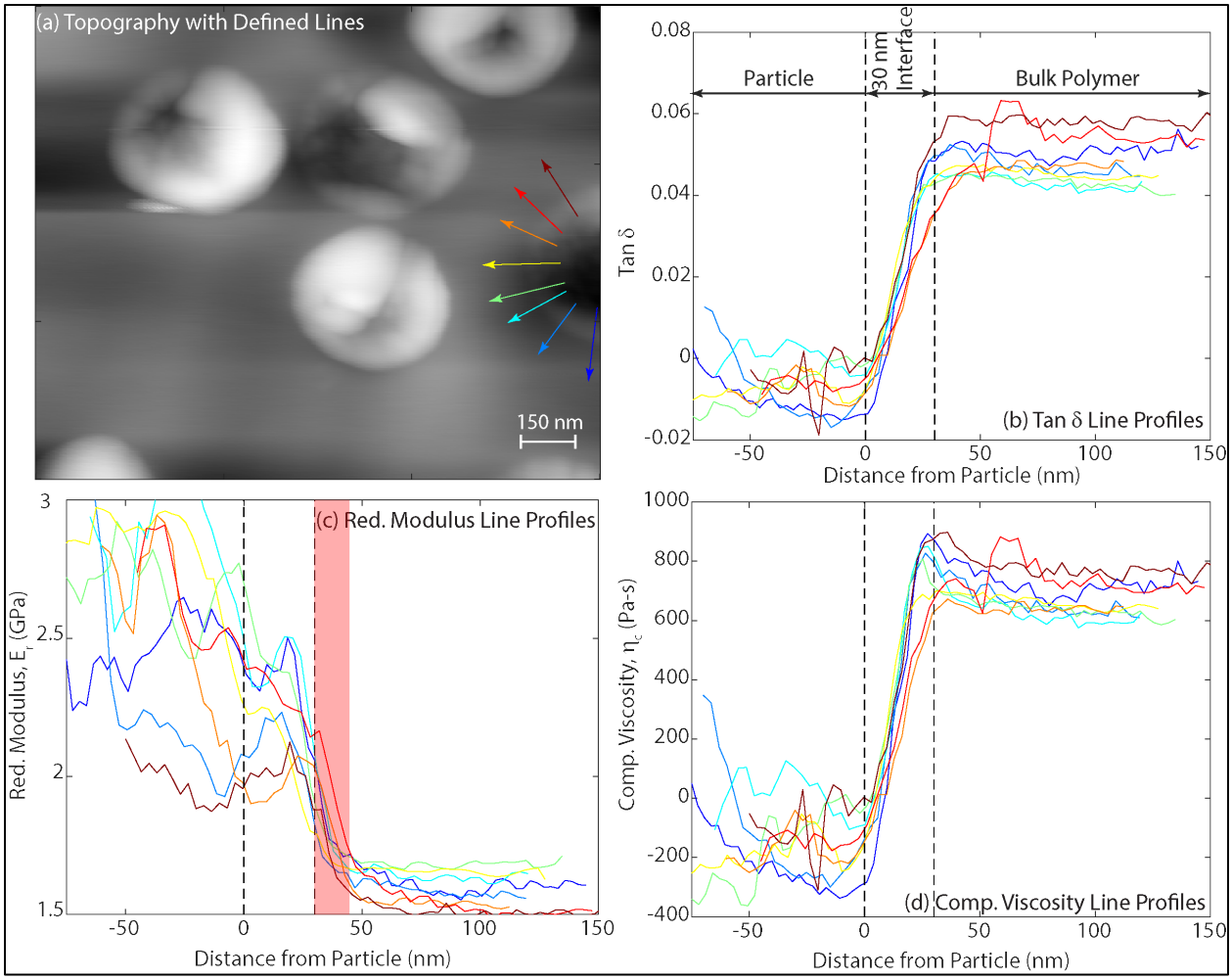


Figure 27. (a) Topography image of cross-sectioned PU-unfunctionalized silica composite showing lines along which profiles are plotted (colored arrows). Profiles along each colored line are shown for (b) tan δ, (c) $E_R$, and (d) $\eta_c$. Colors of arrows in (a) correspond to line colors in (b)–(d). Shaded red region in (c) corresponds to the additional distance the modulus changes outside of the defined interfacial region (dashed lines).

To further explore the possibility of an interfacial region, the phase-contrast and modulus images were compared for the particle of interest in Figure 28. Here, a mask was defined (transparent blue regions in Figure 28) thresholding the phase image to define the particle ($\phi$ of 31.5°). When this mask was overlaid on the modulus image, there was clearly a thin region outside of the mask where the modulus was still significantly higher than for the bulk polymer. Isolating this region and determining its thickness along the particle perimeter gives the thickness distribution in Figure 28 (c), with a maximum at 10 nm. Again, this could be indicative of an interfacial region, but this is not conclusive on the basis of a single observation.

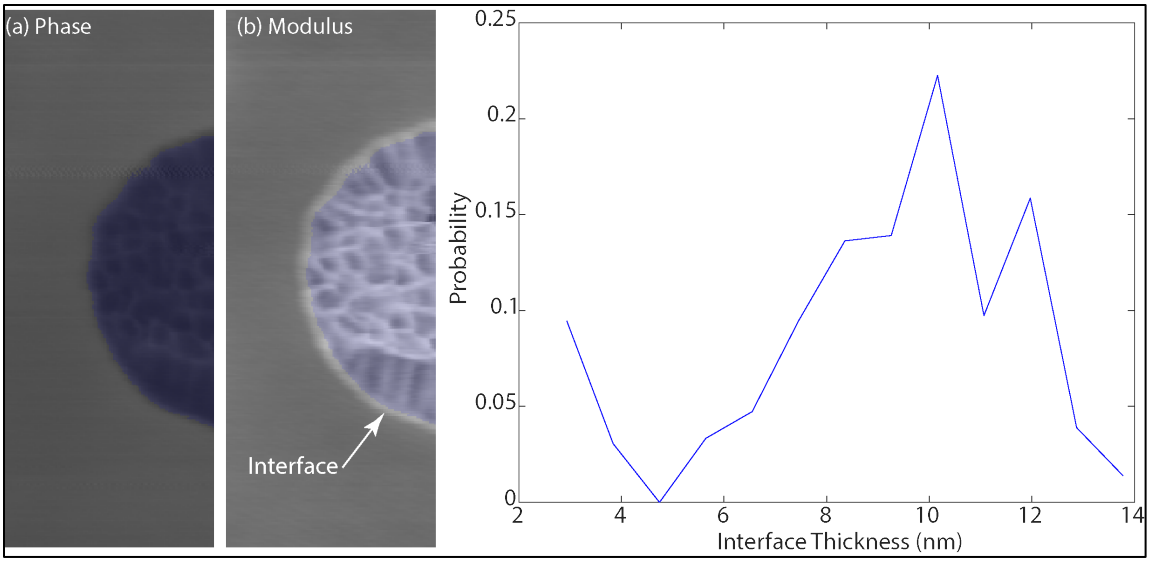


Figure 28. Expanded view of particle analyzed in Figure 27: (a) phase contrast and (b) modulus with overlaid mask (transparent blue) defined by thresholding the phase image. Modulus is higher than the bulk outside of the masked region, which defines an interface region with a thickness distribution shown in (c).

Collinson et al.[51] have presented methods for deconvoluting the contributions from the polymer and particle when the AFM tip is interacting with both simultaneously, to determine the actual extent of an interfacial region in a polymer composite. However, this method relies on imaging the material at multiple indentation depths and normalizing the modulus versus the distance data, which was not done for this data set.

### 3.4.2 Force Spectroscopy Across Interface

In a few cases, force spectroscopy was performed at several points along a line spanning the particle–polymer interface after imaging. Similar to the colloidal force spectroscopy presented in Section 3.3, a force curve is acquired at each point along the line; however, in this case, a sharp AFM tip was used. The tip was the same one used in the imaging ($R_{tip}$ of ~10 nm), rather than the 5 µm silica particle. Figure 29 shows the modulus computed from each force curve along the lines shown on the corresponding topography maps. In one case, the modulus varied over a 10 nm region, while in the other case, it varied over about 30 nm, which is consistent with the AM–FM imaging results shown above. It is important to note that in the case of the 30 nm interface, the polymer was damaged, as shown in Figure 29, which indicates a large indentation. This could mean that the larger interface size detected was due to interaction of the tip with the particle at a further distance from the interface as a result of higher indentation. Similar to the AM–FM imaging, the force spectroscopy was inconclusive in determining the presence of an interfacial region in PU–silica composites.

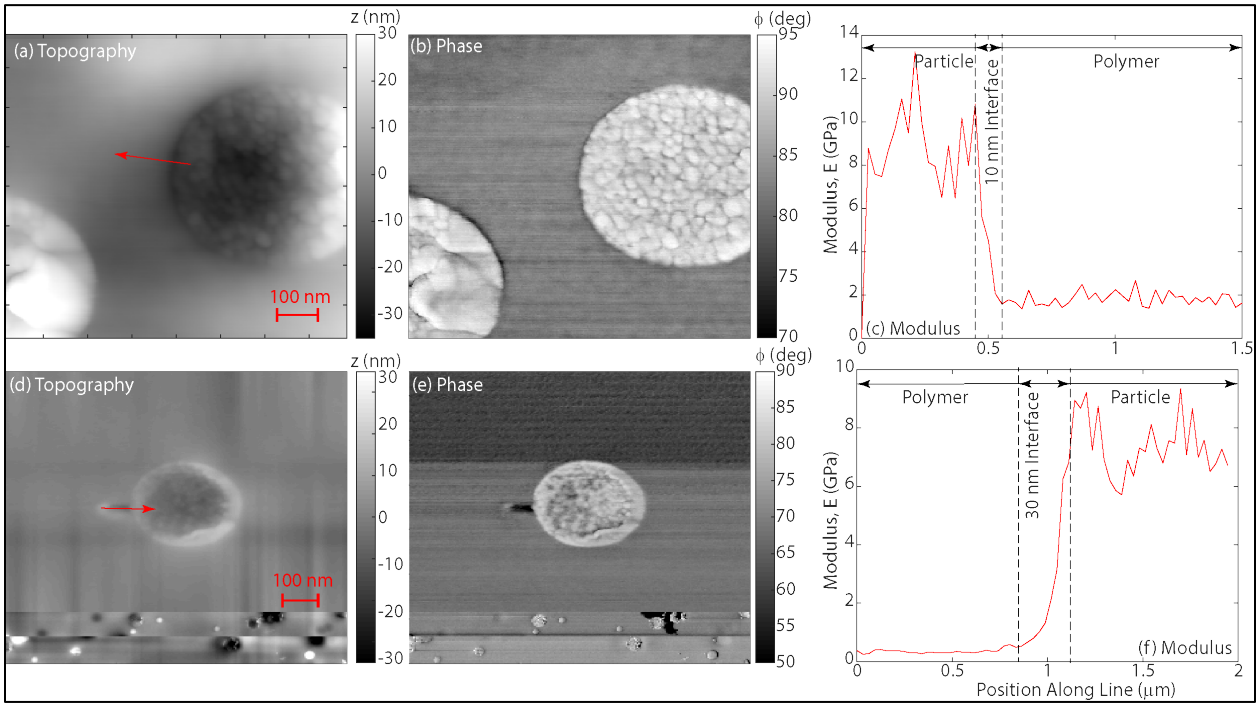


Figure 29. Force spectroscopy along lines (red arrows in (a) and (d)) spanning particle–polymer interface: topography maps (a) and (d), phase contrast (b) and (e), and computed modulus along each line (c) and (f).

## 4. CONCLUSIONS

This work sought to elucidate the role of varying particle–polymer interface properties on chemical breakthrough in high solids loading polymer composites. Based on previous work, it was hypothesized that less interaction of the polymer with the particle surface leads to fast transport pathways via a percolation mechanism in which the "poor" interfaces overlap in high solids loading composites. AFM-based colloidal force spectroscopy and viscoelastic imaging were used to assess the quality of the particle–polymer interface. Unfortunately, results of these studies were inconclusive, and it is unclear how the interface varied in composites with different silica surface chemistries.

Studies of MeOH breakthrough in PU–$SiO_2$ composites suggest two parallel mechanisms: (1) diffusion through the polymer matrix with silica particles acting as barriers, and (2) adsorption of MeOH at the surface of the silica particles.

Overall, using the AFM-based methods for interrogating the particle–polymer interface yielded inconclusive results. There are several considerations for improving upon the work performed here to use AFM imaging to assess interfacial regions in polymer composites:

1. Improve sample preparation techniques to ensure the smoothest possible cross section with minimal disturbance to the particle–polymer interface. This is particularly difficult using a microtome on a composite with hard inclusions

as in this work (silica), which can prevent clean sectioning of the particles and quickly degrades the knife. This can cause displacement and dragging of particles and particle fragments along the surface. Future work should more carefully explore the influence of sectioning conditions (i.e., cryo-stage temperature, slice thickness, and cutting speed). Also, alternatives such as ion polishing and focused ion-beam milling should be investigated during any follow-on work.

2. The composite should be sectioned immediately prior to imaging to prevent surface contamination. At lower indentations, surface contamination becomes a more prominent error source. It would also be beneficial to section the pure polymer prior to colloidal force spectroscopy to ensure a clean, flat surface for adhesion force measurements.
3. The surface chemistry of the particles should be confirmed, for example, with X-ray photoelectron spectroscopy. This was not done for the silica particles in this study, so it is difficult to confidently link the assumed surface chemistry to composite behavior.
4. The variation in particle surface chemistry should be made larger to ensure that the polymer interaction at the interface is sufficiently different. In this work, the carboxyl- and amine-functionalized silica both form H-bonds with the PU chains, and it is expected that the bare silica surface is populated with hydroxyl groups that form similar H-bonds with PU. Colloidal force spectroscopy could be used to screen particle surface chemistries to ensure a sufficient range of particle–polymer surface energies is covered.
5. AFM viscoelastic imaging should be performed at multiple indentations to enable deconvolution of the data, according to the work of Collinson et al.[51] Imaging should start at the lowest amplitude setting and then increase to the level of indentation as the experiment proceeds. Furthermore, tip shape should be determined before and after each experiment using an appropriate calibration grating.
6. Breakthrough experiments should be performed with multiple probe chemicals. Here, only MeOH was used, which interacts to a considerable degree with the silica inclusions in the composite. Probe chemicals that do not interact with the solid inclusions should also be considered.

Blank

## LITERATURE CITED


1. Pearl, T.P.; Mantooth, B.A.; Eikenberg, J.H.; Varady, M.J.; Walker, A.Y.; Van de Voorde, K.M.; Iezzi, E.B.; Camerino, E.; Sweat, M.L.; Stafford, C.M.; Woodcock, J.; Hulet, M.S.; Hinkle, A.R. *Evaluation of Chemical Agent Resistance of Polysiloxane-Based Films and Coatings*; DEVCOM CBC-TR-1797; U.S. Army Combat Capabilities Development Command: Aberdeen Proving Ground, MD, 2022; UNCLASSIFIED Report (AD1182634).
2. Varady, M.J.; Mantooth, B.A. Unsaturated Hemiwicking Dynamics on Surfaces with Irregular Roughness. *J. Colloid Interface Sci* **2021,** *604*, 104–112.
3. Hegde, V.H.; Doherty, M.F.; Squires, T.M. A Two-Phase Model that Unifies and Extends the Classical Models of Membrane Transport. *Science* **2022,** *377* (6602), 186–191.
4. Paul, D.R. Reformulation of the Solution-Diffusion Theory of Reverse Osmosis. *J. Membr. Sci.* **2004,** *241* (2), 371–386.
5. Flory, P.J. Thermodynamics of High Polymer Solutions. *J. Chem. Phys.* **1942,** *10* (1), 51–61.
6. Flory, P.J.; Rehner, J. Statistical Mechanics of Cross-Linked Polymer Networks II. Swelling. *J. Chem. Phys.* **1943,** *11* (11), 521–526.
7. Barton, A.F.M. *CRC Handbook of Polymer-Liquid Interaction Parameters and Solubility Parameters*. CRC Press: Boca Raton, FL, 1990.
8. Sharma, J.; Tewari, K.; Arya, R.K. Diffusion in Polymeric Systems—A Review on Free Volume Theory. *Prog. Org. Coat.* **2017,** *111*, 83–92.
9. Vrentas, J.S.; Duda, J.L. Diffusion of Small Molecules in Amorphous Polymers. *Macromolecules* **1976,** *9* (5), 785–790.
10. Vrentas, J.S.; Vrentas, C.M. Evaluation of Free-Volume Theories for Solvent Self-Diffusion in Polymer Solvent Systems. *J. Polym. Sci. B Polym. Phys.* **1993,** *31* (1), 69–76.
11. Boesel, L.F. Effect of Plasticizers on the Barrier and Mechanical Properties of Biomimetic Composites of Chitosan and Clay. *Carbohydr. Polym.* **2015,** *115*, 356–363.
12. Xie, H.Z.; Wu, L.B.; Li, B.G.; Dubois, P. Modification of Poly(ethylene 2,5-furandicarboxylate) with Aliphatic Polycarbonate Diols: 1. Randomnized Copolymers with Significantly Improved Ductility and High $CO_2$ Barrier Performance. *Eur. Polym. J.* **2020,** *134*, 8.
13. Zhang, H.J.; Sellaiyan, S.; Sako, K.; Uedono, A.; Taniguchi, Y.; Hayashi, K. Effect of Free-Volume Holes on Static Mechanical Properties of Epoxy Resins Studied by Positron Annihilation and PVT Experiments. *Polymer* **2020,** *190*, 9.
14. Hoang, V.T.; Kaliaguine, S. Predictive Models for Mixed-Matrix Membrane Performance: A Review. *Chem. Rev.* **2013,** *113* (7), 4980–5028.
15. Cooley, K.A.; Pearl, T.P.; Varady, M.J.; Mantooth, B.A.; Willis, M.P. Direct Measurement of Chemical Distributions in Heterogeneous Coatings. *ACS Appl. Mater. Interfaces* **2014,** *6* (18), 16289–16296.

16. Mantooth, B.A.; Varady, M.J.; Pearl, T.P.; Cooley, K.A. *Chemical Depth Profiling in Coatings Using Scanning Electron Microscopy and Energy Dispersive Spectroscopy*; ECBC-TR-1472; U.S. Army Edgewood Chemical Biological Center: Aberdeen Proving Ground, MD, 2017; UNCLASSIFIED Report (AD1039338).
17. Boyne, D.A.; Varady, M.J.; Lambeth, R.H.; Eikenberg, J.H.; Bringuier, S.A.; Pearl, T.P.; Mantooth, B.A. Solvent-Assisted Desorption of 2,5-Lutidine from Polyurethane Films. *J. Phys. Chem. B* **2018,** *122* (7), 2155–2164.
18. Rittigstein, P.; Priestley, R.D.; Broadbelt, L.J.; Torkelson, J.M. Model Polymer Nanocomposites Provide an Understanding of Confinement Effects in Real Nanocomposites. *Nat. Mater.* **2007,** *6* (4), 278–282.
19. Baeza, G.P.; Dessi, C.; Costanzo, S.; Zhao, D.; Gong, S.S.; Alegria, A.; Colby, R.H.; Rubinstein, M.; Vlassopoulos, D.; Kumar, S.K. Network Dynamics in Nanofilled Polymers. *Nat. Commun.* **2016,** *7*, 6.
20. Mapesa, E.U.; Street, D.P.; Heres, M.F.; Kilbey, S.M.; Sangoro, J. Wetting and Chain Packing across Interfacial Zones Affect Distribution of Relaxations in Polymer and Polymer-Grafted Nanocomposites. *Macromolecules* **2020,** *53* (13), 5315–5325.
21. Bansal, A.; Yang, H.C.; Li, C.Z.; Cho, K.W.; Benicewicz, B.C.; Kumar, S.K.; Schadler, L.S. Quantitative Equivalence Between Polymer Nanocomposites and Thin Polymer Films. *Nat. Mater.* **2005,** *4* (9), 693–698.
22. Jouault, N.; Crawford, M.K.; Chi, C.Z.; Smalley, R.J.; Wood, B.; Jestin, J.; Melnichenko, Y.B.; He, L.L.; Guise, W.E.; Kumar, S.K. Polymer Chain Behavior in Polymer Nanocomposites with Attractive Interactions. *ACS Macro Lett.* **2016,** *5* (4), 523–527.
23. Jouault, N.; Moll, J. F.; Meng, D.; Windsor, K.; Ramcharan, S.; Kearney, C.; Kumar, S.K. Bound Polymer Layer in Nanocomposites. *ACS Macro Lett.* **2013,** *2* (5), 371–374.
24. Shokoohi, S.; Arefazar, A.; Khosrokhavar, R. Silane Coupling Agents in Polymer-Based Reinforced Composites: A Review. *J. Reinf. Plast. Compos.* **2008,** *27* (5), 473–485.
25. Xie, Y.J.; Hill, C.A.S.; Xiao, Z.F.; Militz, H.; Mai, C. Silane Coupling Agents Used for Natural Fiber/Polymer Composites: A Review. *Compos. Part A Appl. Sci. Manuf.* **2010,** *41* (7), 806–819.
26. Abdelmouleh, M.; Boufi, S.; Belgacem, M.N.; Dufresne, A.; Gandini, A. Modification of Cellulose Fibers with Functionalized Silanes: Effect of the Fiber Treatment on the Mechanical Performances of Cellulose-Thermoset Composites. *J. Appl. Polym. Sci.* **2005,** *98* (3), 974–984.
27. Griswold, C.; Cross, W.M.; Kjerengtroen, L.; Kellar, J.J. Interphase Variation in Silane-Treated Glass-Fiber-Reinforced Epoxy Composites. *J. Adhes. Sci. Technol.* **2005,** *19* (3–5), 279–290.
28. Metin, D.; Tihminhoglu, F.; Balkose, D.; Ulku, S. The Effect of Interfacial Interactions on the Mechanical Properties of Polypropylene/Natural Zeolite Composites. *Compos. Part A Appl. Sci. Manuf.* **2004,** *35* (1), 23–32.
29. Maillard, D.; Kumar, S.K.; Fragneaud, B.; Kysar, J.W.; Rungta, A.; Benicewicz, B.C.; Deng, H.; Brinson, L.C.; Douglas, J.F. Mechanical Properties of Thin Glassy Polymer Films Filled with Spherical Polymer-Grafted Nanoparticles. *Nano Lett.* **2012,** *12* (8), 3909–3914.
30. Wan, Y.J.; Tang, L.C.; Gong, L.X.; Yan, D.; Li, Y.B.; Wu, L.B.; Jiang, J.X.; Lai, G.Q. Grafting of Epoxy Chains onto Graphene Oxide for Epoxy Composites with Improved Mechanical and Thermal Properties. *Carbon* **2014,** *69*, 467–480.

31. Chevigny, C.; Jouault, N.; Dalmas, F.; Boue, F.; Jestin, J. Tuning the Mechanical Properties in Model Nanocomposites: Influence of the Polymer-Filler Interfacial Interactions. *J. Polym. Sci. Part B Polym. Phys.* **2011,** *49* (11), 781–791.
32. Oakey, J.; Marr, D.W.M.; Schwartz, K.B.; Wartenberg, M. An Integrated AFM and SANS Approach Toward Understanding Void Formation in Conductive Composite Materials. *Macromolecules* **2000,** *33* (14), 5198–5203.
33. Kim, S.; Dura, J.A.; Page, K.A.; Rowe, B.W.; Yager, K.G.; Lee, H.J.; Soles, C.L. Surface-Induced Nanostructure and Water Transport of Thin Proton-Conducting Polymer Films. *Macromolecules* **2013,** *46* (14), 5630–5637.
34. Lin, E.K.; Kolb, R.; Satija, S.K.; Wu, W.L. Reduced Polymer Mobility Near the Polymer Solid Interface as Measured by Neutron Reflectivity. *Macromolecules* **1999,** *32* (11), 3753–3757.
35. Sharma, S.K.; Sudarshan, K.; Sahu, M.; Pujari, P.K. Investigation of Free Volume Characteristics of the Interfacial Layer in Poly(methyl methacrylate)-alumina Nanocomposite and Its Role in Thermal Behaviour. *RSC Adv.* **2016,** *6* (72), 67997–68004.
36. Butt, H.J.; Duran, H.; Egger, W.; Faupel, F.; Harmandaris, V.; Harms, S.; Johnston, K.; Kremer, K.; Lin, F.Y.; Lue, L.; Ohrt, C.; Raetzke, K.; Ravelli, L.; Steffen, W.; Vianna, S.D.B. Interphase of a Polymer at a Solid Interface. *Macromolecules* **2014,** *47* (23), 8459–8465.
37. Butt, H.J.; Cappella, B.; Kappl, M. Force Measurements with the Atomic Force Microscope: Technique, Interpretation and Applications. *Surf. Sci. Rep.* **2005,** *59* (1–6), 1–152.
38. Leite, F.L.; Herrmann, P.S.P. Application of Atomic Force Spectroscopy (AFS) to Studies of Adhesion Phenomena: A Review. *J. Adhes. Sci. Technol.* **2005,** *19* (3–5), 365–405.
39. Nguyen, H.K.; Liang, X.B.; Ito, M.; Nakajima, K. Direct Mapping of Nanoscale Viscoelastic Dynamics at Nanofiller/Polymer Interfaces. *Macromolecules* **2018,** *51* (15), 6085–6091.
40. Niu, Y.F.; Yan, Y.; Yao, J.W. Hygrothermal Aging Mechanism of Carbon Fiber/Epoxy Resin Composites Based on Quantitative Characterization of Interface Structure. *Polym. Test* **2021,** *94*, 107019.
41. Varady, M.J.; Boyne, D.A.; Pearl, T.P.; Lambeth, R.H.; Mantooth, B.A. Composition-Dependent Multicomponent Diffusivity of 2,5-Lutidine with Acetonitrile in Polyurethane. *Polymer* **2019,** *180*, 121697.
42. Kocun, M.; Labuda, A.; Meinhold, W.; Revenko, I.; Proksch, R. Fast High Resolution, and Wide Modulus Range Nanomechanical Mapping with Bimoda Tapping Mode. *ACS Nano* **2017,** *11* (10), 10097–10105.
43. Labuda, A.; Kocun, M.; Meinhold, W.; Walters, D.; Proksch, R. Generalized Hertz Model for Bimodal Nanomechanical Mapping. *Beilstein J. Nanotechnol.* **2016,** *7*, 970–982.
44. Zid, S.; Zinet, M.; Espuche, E. Modeling Diffusion Mass Transport in Multiphase Polymer Systems for Gas Barrier Applications: A Review. *J. Polym. Sci. Part B Polym. Phys.* **2018,** *56* (8), 621–638.
45. Zhuravlev, L.T. The Surface Chemistry of Amorphous Silica, Zhuravlev Model. *Colloids Surf. A Physicochem. Eng. Asp.* **2000,** *173* (1–3), 1–38.

46. Morrow, B.A. Infra-Red Studies of Reactions on Oxide Surfaces. Part 2. Methanol on Silica. *J. Chem. Soc. Faraday Trans. 1* **1974,** *70*, (8), 1527–1545.
47. Levine, F.; Escarsega, J.; La Scala, J. Effect of Isocyanate to Hydroxyl Index on the Properties of Clear Polyurethane Films. *Prog. Org. Coat.* **2012,** *74* (3), 572–581.
48. Proksch, R.; Kocun, M.; Hurley, D.; Viani, M.; Labuda, A.; Meinhold, W.; Bemis, J. Practical Loss Tangent Imaging with Amplitude-Modulated Atomic Force Microscopy. *J. Appl. Phys.* **2016,** *119* (13), 134901.
49. Proksch, R.; Yablon, D.G. Loss Tangent Imaging: Theory and Simulations of Repulsive-Mode Tapping Atomic Force Microscopy. *Appl. Phys. Lett.* **2012,** *100* (7), 073106.
50. Benaglia, S.; Amo, C.A.; Garcia, R. Fast, Quantitative and High Resolution Mapping of Viscoelastic Properties with Bimodal AFM. *Nanoscale* **2019,** *11* (32), 15289–15297.
51. Collinson, D.W.; Eaton, M.D.; Shull, K.R.; Brinson, L.C. Deconvolution of Stress Interaction Effects from Atomic Force Spectroscopy Data Across Polymer–Particle Interfaces. *Macromolecules* **2019,** *52* (22), 8940–8955.
52. Collinson, D.W.; Sheridan, R.J.; Palmeri, M.J.; Brinson, L.C. Best Practices and Recommendations for Accurate Nanomechanical Characterization of Heterogeneous Polymer Systems with Atomic Force Microscopy. *Prog. Polym. Sci.* **2021,** *119*, 101420.

## ACRONYMS AND ABBREVIATIONS

| | |
|---|---|
| AFM | atomic force microscopy |
| AM | amplitude modulation |
| ATR | attenuated total reflectance |
| BDS | broadband dielectric spectroscopy |
| CWA | chemical warfare agent |
| DDTMS | dodecyltrimethoxysilane |
| DMA | dynamic mechanical analysis |
| DSC | differential scanning calorimetry |
| DI | deionized |
| EDS | energy-dispersive spectroscopy |
| EtOH | ethanol |
| $F_{adh}$ | adhesion force |
| FM | frequency modulation |
| FTIR | Fourier transform infrared spectroscopy |
| HATR | horizontal attenuated total reflectance |
| JKR | Johnson–Kendall–Roberts |
| MeOH | methanol |
| P2VP | poly(2-vinyl pyridine) |
| PALS | positron annihilation lifetime spectroscopy |
| PMMA | polymethylmethacrylate |
| PS | polystyrene |
| PU | polyurethane |
| SEM | scanning electron microscopy |
| $T$g | glass-transition temperature |
| THF | tetrahydrofuran |

Blank

## DISTRIBUTION LIST

The following individuals and organizations were provided with one electronic version of this report:

U.S. Army Combat Capabilities Development Command
Chemical Biological Center
(DEVCOM CBC)
Decontamination Sciences Branch
FCDD-CBR-PD
ATTN: Pearl, T.
Morrisey, K.
FCDD-CBR
ATTN: McDaniel, P.

DEVCOM CBC Technical Library
FCDD-CBR-L
ATTN: Foppiano, S.
Stein, J.

Defense Technical Information Center
ATTN: DTIC OA

# U.S. ARMY


U.S. ARMY COMBAT CAPABILITIES DEVELOPMENT COMMAND
CHEMICAL BIOLOGICAL CENTER